In this normalized correction the attenuation by air scatter is not fully corrected for each pixel, but rather corrected to the same attenuation level as the pixel in the detector centre. This means that the effect of path-length differences between the detector centre pixel and other pixels are eliminated.

2.5.3.3.6. *Sample absorption*

The absorption of X-rays by the sample reduces the diffracted intensity. Many approaches are used to calculate and correct the absorption effect for various sample shapes and geometries [*International Tables for Crystallography* Volume C, Chapter 6.3 (Maslen, 1992); Ross, 1992; Pitschke *et al.*, 1996; Zuev, 2006]. The sample absorption can be measured by the transmission coefficient (also referred to as the absorption factor):

$$A = (1/V) \int_V \exp(-\mu\tau)\, \mathrm{d}V, \tag{2.5.32}$$

where A is the transmission coefficient, μ is the linear absorption coefficient and τ is the total beam path in the sample, which includes the incident-beam path and diffracted-beam path. Fig. 2.5.15(a) shows reflection-mode diffraction with a flat-plate sample. The thickness of the plate is t. z is the distance of the element $\mathrm{d}V$ from the sample surface. The normal to the reflection surface is **n**. The incident beam is represented by the unit vector $\mathbf{s}_o$ and the diffracted beam by the unit vector **s**. The transmission coefficient is given as (Maslen, 1992)

$$A = \frac{1 - \exp\{-\mu t[(1/\cos\eta) + (1/\cos\zeta)]\}}{\mu[(\cos\zeta/\cos\eta) + 1]}, \tag{2.5.33}$$

where η is the angle between the incident beam and the normal to the sample surface, and ζ is the angle between the diffracted beam and the sample normal. For two-dimensional X-ray diffraction, there is a single incident-beam direction at a time, but various diffracted-beam directions simultaneously, so

$$\cos\eta = \sin\omega\cos\psi \tag{2.5.34}$$

and

$$\cos\zeta = -\cos 2\theta \sin\omega\cos\psi - \sin 2\theta \sin\gamma\cos\omega\cos\psi - \sin 2\theta\cos\gamma\sin\psi. \tag{2.5.35}$$

The transmission coefficient from equation (2.5.33) contains a length unit, which creates ambiguity if such transmission coefficients are used to correct the intensity pixel-by-pixel. In order to make the relative intensity comparable to the results from Bragg–Brentano geometry, we introduce a new transmission coefficient, which is normalized by the transmission coefficient of the Bragg–Brentano geometry, $A_{\mathrm{BB}} = 1/(2\mu)$. This normalized transmission coefficient is also a numerical factor without units. The transmission coefficient with normalization will be denoted by T hereafter in this chapter. The transmission coefficient for reflection-mode diffraction with a flat sample of thickness t is then given as

$$T = A/A_{\mathrm{BB}} = \frac{2\cos\eta\big(1 - \exp\{-\mu t[(1/\cos\eta) + (1/\cos\zeta)]\}\big)}{\cos\eta + \cos\zeta}. \tag{2.5.36}$$

For a thick plate or material with a very high linear absorption coefficient, the transmission through the sample thickness is negligible and the above equation becomes

$$T = \frac{2\cos\eta}{\cos\eta + \cos\zeta}. \tag{2.5.37}$$

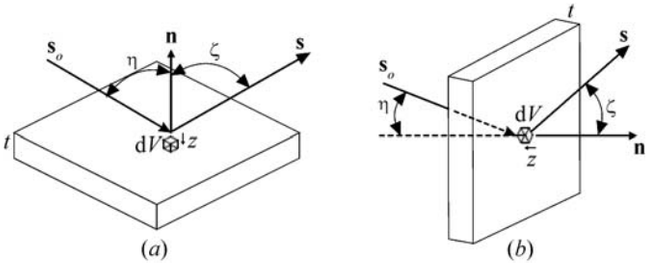

Figure 2.5.15
Absorption correction for a flat slab: (a) reflection; (b) transmission.

Fig. 2.5.15(b) shows transmission-mode diffraction with a flat-plate sample. The thickness of the plate is t. The normal to the reflection surface is represented by the unit vector **n**. The incident beam is represented by the unit vector $\mathbf{s}_o$ and the diffracted beam by the unit vector **s**. η is the angle between the incident beam and the normal of the sample surface, and ζ is the angle between the diffracted beam and the sample normal.

The transmission coefficient normalized by $A_{\mathrm{BB}} = 1/(2\mu)$ is given by (Maslen, 1992; Ross, 1992)

$$T = \frac{2\sec\eta[\exp(-\mu t\sec\eta) - \exp(-\mu t\sec\zeta)]}{\sec\zeta - \sec\eta} \quad \text{for } \sec\zeta \neq \sec\eta. \tag{2.5.38}$$

For two-dimensional X-ray diffraction in transmission mode

$$\cos\eta = \sin\omega\sin\psi\sin\varphi + \cos\omega\cos\varphi \tag{2.5.39}$$

and

$$\cos\zeta = (\sin\omega\sin\psi\sin\varphi + \cos\omega\cos\varphi)\cos 2\theta + (\cos\omega\sin\psi\sin\varphi - \sin\omega\cos\varphi)\sin 2\theta\sin\gamma - \cos\psi\sin\varphi\sin 2\theta\cos\gamma. \tag{2.5.40}$$

It is very common practice to set the incident angle perpendicular to the sample surface, *i.e.* $\eta = 0$. For most transmission-mode data collection, equation (2.5.40) becomes

$$T = \frac{2[\exp(-\mu t) - \exp(-\mu t\sec\zeta)]}{\sec\zeta - 1}. \tag{2.5.41}$$

When $\eta = \zeta$, both the numerator and denominator approach zero, and the transmission coefficient should be given by

$$T = 2\mu t\sec\zeta\exp(-\mu t\sec\zeta). \tag{2.5.42}$$

It is common practice to load the sample perpendicular to the incident X-ray beam at the goniometer angles $\omega = \psi = \varphi = 0$. Therefore, $\cos\eta = 1$ and $\cos\zeta = \cos 2\theta$, and the transmission coefficient becomes

$$T = \frac{2\cos 2\theta[\exp(-\mu t) - \exp(-\mu t/\cos 2\theta)]}{1 - \cos 2\theta}. \tag{2.5.43}$$

The maximum scattered intensity occurs when

$$t = \frac{\cos 2\theta \ln\cos 2\theta}{\mu(\cos 2\theta - 1)}. \tag{2.5.44}$$

This equation can be used to select the optimum sample thickness for transmission-mode diffraction. For example, if the measurement 2θ range is between 3 and 50°, the preferred sample thickness should be given by μt = 0.8–1.0.

2.5.4. Applications

2.5.4.1. *Phase identification*

In materials science, a phase is defined as a region that has uniform chemical composition and physical properties, including crystal structure. Therefore, every phase should give a unique diffraction pattern. A sample for X-ray diffraction may contain a single phase or multiple phases. Analysis of the diffraction pattern can accurately and precisely determine the contents of the sample. This qualitative analysis is called phase identification (phase ID). One of the most efficient methods of phase identification is to compare the diffraction pattern from an unknown material to those in a database of a large number of standard diffraction patterns. The most comprehensive database is the Powder Diffraction File (PDF), updated annually by the International Centre for Diffraction Data (ICDD).

Two-dimensional X-ray diffraction has enhanced phase identification in many respects (Rudolf & Landes, 1994; Sulyanov *et al.*, 1994; Hinrichsen, 2007). Because of its ability to collect diffracted X-rays in a large angular range in both the 2θ and γ directions, it can collect diffraction data with high speed and better sampling statistics than obtained by conventional diffraction. Owing to point-beam illumination on the sample, a relatively small sample size is required for phase identification. The large 2D detector allows for a large 2θ range to be analysed without any movement of the sample and detector. This makes it possible to perform *in situ* phase investigation on samples during phase transformations, chemical reactions and deformations. The diffraction information in the γ direction allows accurate phase identification of samples with large grains and preferred orientation.

In the Bragg–Brentano geometry, the 2θ resolution is controlled by the selection of the divergence slit and receiving slit in the diffractometer plane, and the axial divergence is controlled by Soller slits, while in a diffractometer with a 2D detector, the 2θ resolution is mainly determined by the spatial resolution of the detector and the sample-to-detector distance. The relative peak intensity in a diffraction pattern from a sample with texture measured with a 2D detector can be significantly different from the results measured with Bragg–Brentano geometry. It is imperative to study the nature of these discrepancies so that the diffraction patterns collected with 2D detectors can be used for phase ID with proper understanding and correction if necessary.

When two-dimensional diffraction is used for phase identification, the first step is to integrate the 2D diffraction frame into a diffraction profile resembling the diffraction pattern collected with a conventional diffractometer (Cervellino *et al.*, 2006; Rodriguez-Navarro, 2006; Boesecke, 2007; Fuentes-Montero *et al.*, 2011; Hammersley, 2016). The integrated diffraction profiles can be analysed with all existing algorithms and methods, including profile fitting with conventional peak shapes and fundamental parameters, quantification of phases, and lattice-parameter determination and refinement (Ning & Flemming, 2005; Flemming, 2007; Jabeen *et al.*, 2011). The results can be used to search a powder-diffraction database to find possible matches. Since there is a great deal of literature covering these topics (Cullity, 1978; Jenkins & Snyder, 1996; Pecharsky & Zavalij, 2003), this section will focus on the special characteristics of two-dimensional X-ray diffraction as well as system geometry, data-collection strategies and data analysis in dealing with relative peak intensities, 2θ resolution, grain size and distribution, and preferred orientation. Many factors and correction algorithms described here can help in understanding the characteristics of two-dimensional diffraction. In most applications, however, the γ-integrated profile can be used for phase identification without these corrections.

2.5.4.1.1. *Relative intensity*

The integrated intensity diffracted from polycrystalline materials with a random orientation distribution is given by

$$I_{hkl} = k_I \frac{p_{hkl}}{v^2}(\mathrm{LPA})\lambda^3 F_{hkl}^2 g_{hkl}(\alpha, \beta)\exp(-2M_t - 2M_s), \quad (2.5.45)$$

where k_I is an instrument constant that is a scaling factor between the experimental observed intensities and the calculated intensity, p_{hkl} is the multiplicity factor of the crystal plane (hkl), v is the volume of the unit cell, (LPA) is the Lorentz–polarization and absorption factors, λ is the X-ray wavelength, F_{hkl} is the structure factor for the crystal plane (hkl), $g_{hkl}(\alpha, \beta)$ is the normalized pole-density distribution function and $\exp(-2M_t - 2M_s)$ is the attenuation factor due to lattice thermal vibrations and weak static displacements (Warren, 1990; He *et al.*, 1994). Except for the texture effect, all the factors in the above equation are either discussed in the previous sections or have the same definitions and values as in conventional diffraction.

Phase-identification studies by XRD are preferably carried out on powders or polycrystalline samples with a random orientation distribution of crystallites. Preferred orientation causes relative intensities to deviate from theoretical calculations or those reported in reference databases. In practice, a sample with a perfectly random orientation distribution of crystallites is very hard to fabricate and most polycrystalline samples have a preferred orientation to a certain extent. Discrepancies in the relative peak intensities between conventional diffraction and 2D-XRD are largely due to texture effects. For B-B geometry, the diffraction vector is always perpendicular to the sample surface. With a strong texture, it is possible that the pole density of certain reflections in the sample normal direction is very low or even approaches zero. In this case, the peak does not appear in the diffraction pattern collected in B-B geometry. In 2D-XRD, several diffraction rings may be measured with a single incident beam; the corresponding diffraction vectors are not necessarily in the sample normal direction. The diffraction profiles from 2D frames are produced by γ integration, therefore the texture factor $g_{hkl}(\alpha, \beta)$ should be replaced by the average normalized pole-density function within the γ integration range $\langle g_{hkl}(\Delta\gamma)\rangle$. The relation between (α, β) and $(2\theta, \gamma)$ is given in Chapter 5.4. The chance of having zero pole density over the entire γ-integration range is extremely small. Therefore, phase identification with 2D-XRD is much more reliable than with conventional diffraction.

2.5.4.1.2. *Detector distance and resolution*

The 2θ resolution with B-B geometry is controlled by the size of the slits. Smaller apertures of the divergence slit are used for higher 2θ resolution and larger apertures for fast data collection. With a two-dimensional X-ray diffraction system, the 2θ resolution is achieved with different approaches. A flat 2D detector has the flexibility to be used at different sample-to-detector distances. The detector resolution is determined by the pixel size and point-spread function. For the same detector resolution and detector active area, a higher resolution can be achieved at larger distance, and higher angular coverage at shorter distance. The sample-to-detector distance should be optimized depending on the 2θ measurement range and required resolution. In situations where the 2θ range of one frame is not enough, several frames at

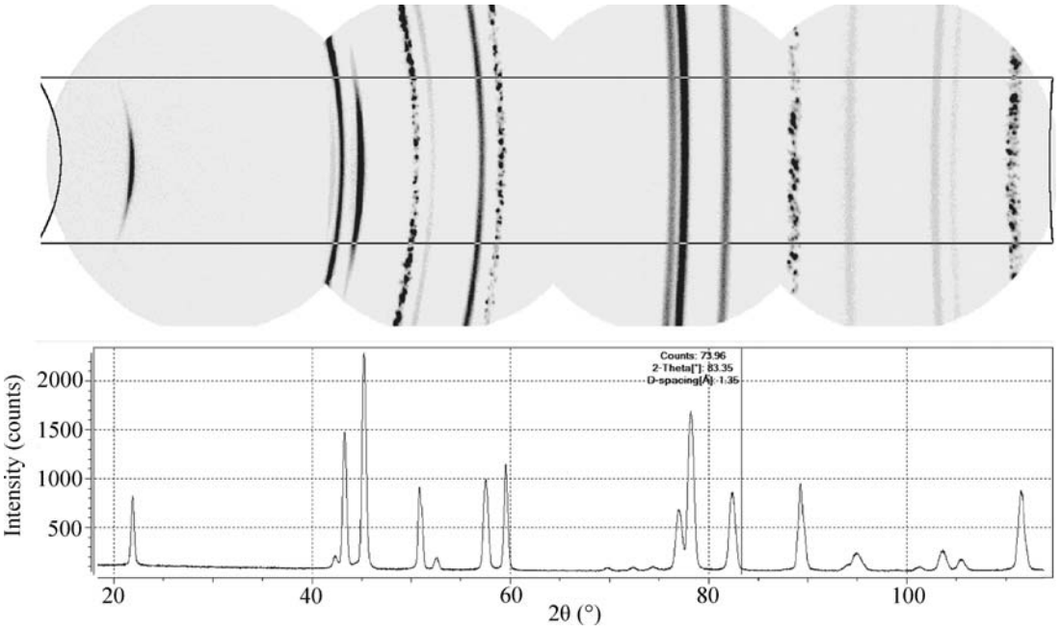

Figure 2.5.16
Diffraction pattern merged from four 2D frames collected from a battery material.

sequential 2θ ranges can be collected. The integrated profiles can then be merged to achieve a large 2θ range. Fig. 2.5.16 shows four 2D frames collected from a battery material with a microgap detector. The slice integration region is defined by two conic lines and two horizontal lines. The diffraction profile integrated from the merged frames is displayed below.

2.5.4.1.3. *Defocusing effect*

A 2D diffraction pattern over a range of 2θ is measured simultaneously with a single incident angle, so the incident angle has to be lower than the minimum 2θ angle. Since the reflected angle cannot always be the same as the incident angle, geometric aberrations are observed. The defocusing effect occurs when the incident angle is lower than the reflection angle. At low incident angles, the incident beam spreads over the sample surface into an area much larger than the size of the original X-ray beam. The observed diffracted beam size is magnified by the defocusing effect if the diffracted beam makes an angle larger than the incident angle. The defocusing effect for reflection-mode diffraction can be expressed as

$$\frac{B}{b} = \frac{\sin\theta_2}{\sin\theta_1} = \frac{\sin(2\theta - \omega)}{\sin\omega}, \qquad (2.5.46)$$

where θ_1 is the incident angle, b is the incident beam size and B is diffracted beam size. The ratio of B to b is a measurement of the geometric aberration and will be referred to as the defocusing factor. In principle, defocusing occurs only when B/b is larger than 1. The reflected beam is actually focused to the detector when $\theta_2 < \theta_1$. The defocusing effect occurs when $\theta_2 > \theta_1$ and the defocusing factor increases with increasing θ_2 or decreasing θ_1. The maximum defocusing appears at $\theta_2 = 90^\circ$. For the θ–2θ configuration, the incident angle ω (= θ_1) is used in the equation.

For B-B geometry with a divergent slit and receiving slit of the same size the defocusing factor is always 1. With a 2D detector the defocusing factor varies with the 2θ angle. If a large 2θ range is measured on a flat sample in reflection mode, it is always desirable to collect several frames at different incident angles for each 2θ range so as to improve the 2θ resolution. A cylindrical detector may collect a diffraction pattern over a large 2θ range (Gelfi *et al.*, 2005). However, the defocusing effect prevents it from being used for a large 2θ range for a flat sample. Fig. 2.5.17 compares the effect for a flat detector and a cylindrical detector. Fig. 2.5.17(*a*) shows a cylindrical detector being used to collect a diffraction pattern from a flat sample for a 2θ range of 5 to 80°. The incident angle must be kept at 5° or lower. Fig. 2.5.17(*b*) shows a flat detector being used to collect the diffraction pattern over the same 2θ range. In order to minimize the defocusing effect, the data collection is done at four different incident angles (5, 15, 25 and 35°) with four corresponding detector swing angles (10, 30, 50 and 70°). Fig. 2.5.17(*c*) compares the defocusing factors of the two configurations. The horizontal dot-dashed line with defocusing factor B/b = 1 represents the situation with B-B geometry. The defocusing factor continues to increase with 2θ angle up to B/b = 11 for cylindrical detector. That means that the 2θ resolution would be 10 times worse than for the B-B geometry. For the diffraction pattern collected with a flat detector in four steps, the defocusing factor fluctuates above 1, with the worst value being less than 3. Another approach to avoiding defocusing is to collect the diffraction pattern in transmission mode. There is no defocusing effect in transmission when the incident beam is perpendicular to the sample surface. Therefore, the transmission pattern has significantly better 2θ resolution. Transmission-mode diffraction also has other advantages. For instance, the air scattering from the primary beam may be blocked by a flat sample, therefore lowering the background from air scattering. However, transmission-mode diffraction data can only be collected from samples with limited thickness, and the maximum scattering intensity is achieved at low 2θ angles with a sample thickness of $t = 1/\mu$, where μ is the linear absorption coefficient. The scattering intensity drops dramatically when the thickness increases.

2.5.4.1.4. *Sampling statistics*

In powder X-ray diffraction, the number of crystallites contributing to each reflection must be sufficiently large to generate reproducible integrated peak intensities (see Chapter 2.10). A larger number of contributing crystallites gives better precision or sampling statistics (also referred to as particle

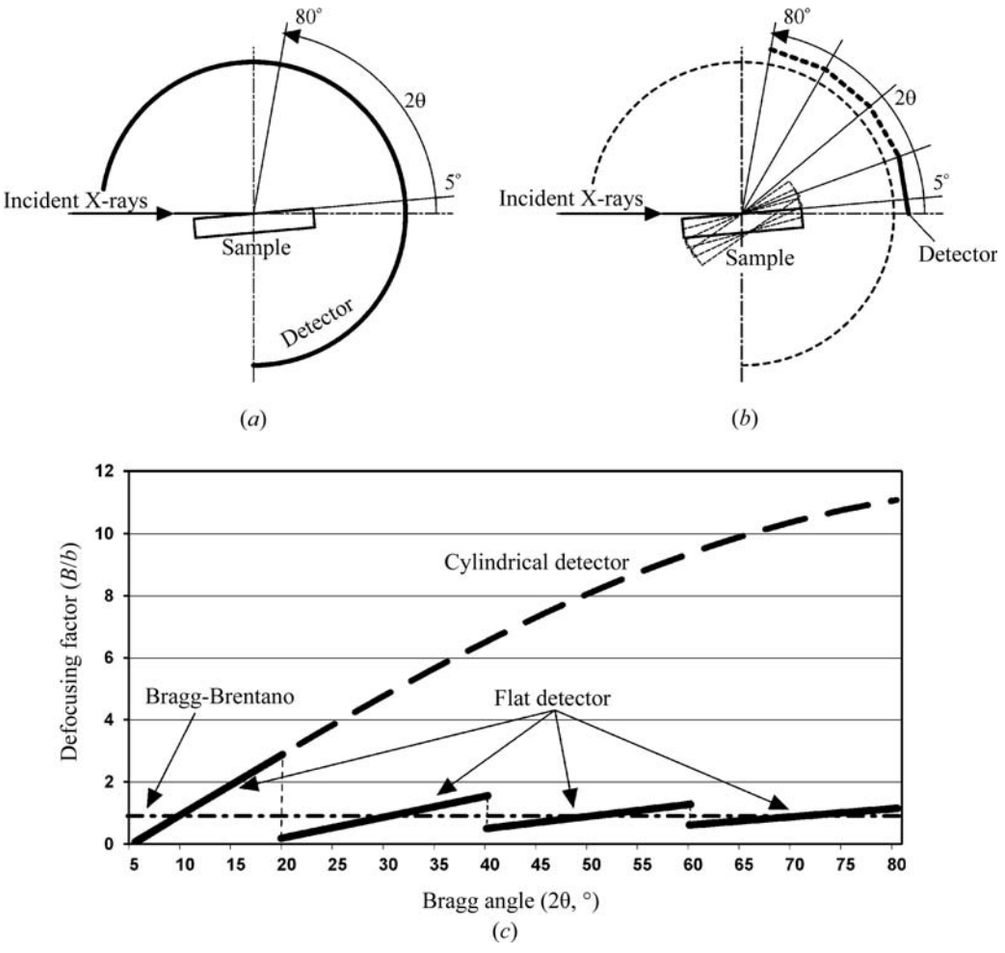

Figure 2.5.17
Defocusing effects: (*a*) cylindrical detector; (*b*) flat detector at various incident angles and detector swing angles; (*c*) comparison of defocusing factors.

statistics). Sampling statistics are determined by both the structure of the sample and the instrumentation. For a powder sample in which the crystallites are perfectly randomly oriented, the number of contributing crystallites for a diffraction peak can be given as

$$N_s = p_{hkl}\frac{Vf_i}{v_i}\frac{\Omega}{4\pi}, \tag{2.5.47}$$

where p_{hkl} is the multiplicity of the diffracting planes, V is the effective sampling volume, f_i is the volume fraction of the measuring crystallites (f_i = 1 for single-phase materials), v_i is the volume of individual crystallites and Ω is the angular window of the instrument (given as a solid angle). The multiplicity term, p_{hkl}, effectively increases the number of crystallites contributing to the integrated intensity from a particular set of (hkl) planes. The volume of individual crystallites, v_i, is an average of various crystallite sizes. The combination of the effective sampling volume and the angular window makes up the instrumental window, which determines the total volume of polycrystalline material making a contribution to a Bragg reflection. For 2D-XRD, the instrumental window is not only determined by the incident beam size and divergence, but also by the detective area and the sample-to-detector distance (γ angular coverage).

In B-B geometry, the effective irradiated volume is a constant,

$$V_{\rm BB} = A_o A_{\rm BB} = A_o/2\mu, \tag{2.5.48}$$

where A_o is the cross-section area of the incident beam measured on the sample surface, $A_{\rm BB} = 1/(2\mu)$ is the transmission coefficient for B-B geometry, and μ is the linear absorption coefficient. For 2D-XRD, the effective volume is given as

$$V = A_o A = A_o T/2\mu, \tag{2.5.49}$$

where A is the transmission coefficient and T is the transmission coefficient with B-B normalization for either transmission or reflection as given previously.

The angular window is given as a solid angle. The incident beam has a divergence angle of β_1 within the diffraction plane and β_2 in the perpendicular direction. The angular window corresponding to the incident-beam divergence is given by

$$\Omega = \beta_1\beta_2/\sin\theta \text{ or } \Omega = \beta^2/\sin\theta \text{ if } \beta = \beta_1 = \beta_2. \tag{2.5.50}$$

For 2D-XRD, the angular window is not only determined by the incident-beam divergence, but also significantly increased by γ integration. When γ integration is used to generate the diffraction profile, it actually integrates the data collected over a range of various diffraction vectors. Since the effect of γ integration on sampling statistics is equivalent to the angular oscillation on the ψ axis in a conventional diffractometer, the effect is referred to as virtual oscillation and $\Delta\psi$ is the virtual oscillation angle. In conventional oscillation, mechanical movement may result in some sample-position error. Since there is no actual physical movement of the sample stage during data collection, virtual oscillation can avoid this error. This is crucial for microdiffraction. The angular window with the contributions of both the incident-beam divergence and the virtual oscillation is

$$\Omega = \beta\Delta\psi = 2\beta\arcsin[\cos\theta\sin(\Delta\gamma/2)], \tag{2.5.51}$$

where β is the divergence of the incident beam. While increasing the divergence angle β may introduce instrumental broadening which deteriorates the 2θ resolution, virtual oscillation improves sampling statistics without introducing instrumental broadening.

In the cases of materials with a large grain size or preferred orientation, or of microdiffraction with a small X-ray beam size, it can be difficult to determine the 2θ position because of poor counting statistics. In these cases, some kind of sample oscillation, either by translation or rotation, can bring more crystallites into the diffraction condition. Angular oscillation is an enhancement to the angular window of the instrument. The effect is that the angular window scans over the oscillation angle. Any of the three rotation angles (ω, ψ, φ) or their combinations can be used as oscillation angles. Angular oscillation can effectively improve the sampling statistics for both large grain size and preferred orientation. As an extreme example, a powder-diffraction pattern can be generated from single-crystal sample if a sufficient angular window can be achieved by sample rotation in such as way as to simulate a Gandolfi camera (Guggenheim, 2005). Sample oscillation is not always necessary if virtual oscillation can achieve sufficient sampling statistics.

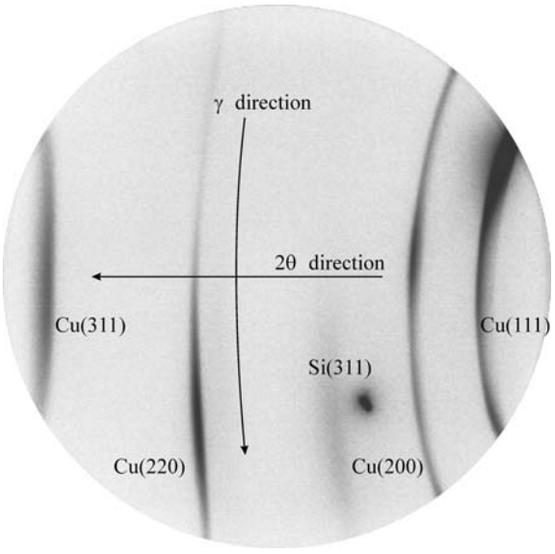

Figure 2.5.18
Diffraction frame collected from a Cu film on an Si substrate showing intensity variation along γ due to texture.

2.5.4.2. *Texture analysis*

Most natural or artificial solid materials are polycrystalline, consisting of many crystallites (also called grains) of various sizes, shapes and orientations. When the orientations of the crystallites in a material have a random distribution, it presents isotropic properties. The anisotropic orientation distribution of crystallites is referred to as preferred orientation or texture. Depending on the degree of the preferred orientation, a sample is referred to as having a weak, moderate or strong texture. Many electrical, optical or mechanical properties of materials are affected or determined by their texture. The determination and interpretation of textures are therefore of fundamental importance in materials science and technology (Bunge, 1983).

When a conventional X-ray diffractometer with a point detector is used for texture measurement, the crystallite orientation distribution in one direction is measured at a time, and full texture information is measured by rotating the sample to all the desired orientations. When a two-dimensional X-ray diffraction system is used for texture measurement, the orientation distributions of several crystallographic planes over a range of angles can be measured simultaneously so as to get better measurement results in a shorter data-collection time (Smith & Ortega, 1993; Blanton, 1994; Bunge & Klein, 1996; Helming *et al.*, 2003; Wenk & Grigull, 2003; He, 2009). The orientation relationships between different phases or between different layers of thin films and substrates can also be easily revealed. The texture effect may be observed and evaluated directly from the 2D diffraction frames without data processing.

2.5.4.2.1. *Pole density and pole figures*

XRD results from an 'ideal' powder in which the crystallites are randomly oriented normally serve as a basis for determining the relative intensity of each diffraction peak. The deviation of the grain orientation distribution of a polycrystalline material from that of an ideal powder is measured as texture. The pole figure for a particular crystallographic plane is normally used to represent the texture of a sample. Assuming that all grains have the same volume, each 'pole' represents a grain that satisfies the Bragg condition. The number of grains satisfying the Bragg condition at a particular sample orientation can be larger or smaller than the number of grains for an ideal sample, and likewise for the integrated intensity of that peak. The measured 2D diffraction pattern contains two very important parameters at each γ angle: the partially integrated intensity I and the Bragg angle 2θ. Fig. 2.5.18 shows a 2D frame for a Cu thin film on an Si wafer collected with a microgap 2D detector. It contains four Cu lines and one Si spot. The diffraction intensity varies along γ because of the anisotropic pole-density distribution. For each diffraction ring, the intensity is a function of γ and the sample orientation (ω, ψ, φ), *i.e.* $I = I(\gamma, \omega, \psi, \varphi)$.

Plotting the intensity of each (hkl) line with respect to the sample coordinates in a stereographic projection gives a qualitative view of the orientation of the crystallites with respect to a sample direction. These stereographic projection plots are called pole figures. As is shown in Fig. 2.5.19(a), the sample orientation is defined by the sample coordinates S_1, S_2 and S_3. For metals with rolling texture, the axes S_1, S_2 and S_3 correspond to the transverse direction (TD), rolling direction (RD) and normal direction (ND), respectively. Let us consider a sphere with unit radius and the origin at O. A unit vector representing an arbitrary pole direction starts from the origin O and ends at the point P on the sphere. The pole direction is defined by the radial angle α and azimuthal angle β. The pole density at the point P projects to the point P' on the equatorial plane through a straight line from P to the point S. The pole densities at all directions are mapped onto the equatorial plane by stereographic projection as shown in Fig. 2.5.19(b). This two-dimensional mapping of the pole density onto the equatorial plane is called a pole figure. The azimuthal angle β projects to the pole figure as a rotation angle about the centre of the pole figure from the sample direction S_1. When plotting the pole density into a pole figure of radius R, the location of the point P' in the pole figure should be given by β and

$$r = R\tan\left(\frac{\pi}{4} - \frac{\alpha}{2}\right) = R\tan\frac{\chi}{2}. \qquad (2.5.52)$$

For easy computer plotting and easy angular readout from the pole figure, the radial angle α may be plotted on an equally spaced angular scale, similar to a two-dimensional polar coordinate system. Other pole-figure mapping styles may be used, but must be properly noted to avoid confusion (Birkholz, 2006).

2.5.4.2.2. *Fundamental equations*

The α and β angles are functions of $\gamma, \omega, \psi, \varphi$ and 2θ. As shown in Fig. 2.5.19(*a*), a pole has three components h_1, h_2 and h_3, parallel to the three sample coordinates S_1, S_2 and S_3, respectively. The pole-figure angles (α, β) can be calculated from the unit-vector components by the following pole-mapping equations:

$$\alpha = \sin^{-1}|h_3| = \cos^{-1}(h_1^2 + h_2^2)^{1/2}, \tag{2.5.53}$$

$$\beta = \pm\cos^{-1}\frac{h_1}{(h_1^2 + h_2^2)^{1/2}} \qquad \begin{cases} \beta \geq 0^\circ \text{ if } h_2 \geq 0 \\ \beta < 0^\circ \text{ if } h_2 < 0 \end{cases}, \tag{2.5.54}$$

where α takes a value between 0 and 90° ($0^\circ \leq \alpha \leq 90^\circ$) and β takes values in two ranges ($0^\circ \leq \beta \leq 180^\circ$ when $h_2 > 0$ and $-180^\circ \leq \beta < 0^\circ$ when $h_2 < 0$). The condition for reflection-mode diffraction is $h_3 > 0$. For transmission diffraction it is possible that $h_3 < 0$. In this case, the pole with mirror symmetry about the S_1S_2 plane to the diffraction vector is used for the pole-figure mapping. The absolute value of h_3 is then used in the equation for the α angle. When $h_2 = 0$ in the above equation, β takes one of two values depending on the value of h_1 ($\beta = 0^\circ$ when $h_1 \geq 0$ and $\beta = 180^\circ$ when $h_1 < 0$). For Eulerian geometry, the unit-vector components $\{h_1, h_2, h_3\}$ are given by equation (2.5.11).

The 2θ integrated intensity along the diffraction ring is then converted to the pole-density distribution along a curve on the pole figure. The α and β angles at each point of this curve are calculated from ω, ψ, φ, γ and 2θ. The sample orientation (ω, ψ, φ) and 2θ for a particular diffraction ring are constants; only γ takes a range of values depending on the detector size and distance.

For a textured sample, the 2θ-integrated intensity of a diffraction ring from a family of (hkl) planes is a function of γ and the sample orientation (ω, ψ, φ), *i.e.* $I_{hkl} = I_{hkl}(\omega, \psi, \varphi, \gamma, \theta)$. From the pole-figure angle-mapping equations, we can obtain the integrated intensity in terms of pole-figure angles as

$$I_{hkl}(\alpha, \beta) = I_{hkl}(\omega, \psi, \varphi, \gamma, \theta). \tag{2.5.55}$$

The pole density at the pole-figure angles (α, β) is proportional to the integrated intensity at the same angles:

$$P_{hkl}(\alpha, \beta) = K_{hkl}(\alpha, \beta) I_{hkl}(\alpha, \beta), \tag{2.5.56}$$

where $I_{hkl}(\alpha, \beta)$ is the 2θ-integrated intensity of the (hkl) peak corresponding to the pole direction (α, β), $K_{hkl}(\alpha, \beta)$ is the scaling factor covering the absorption, polarization, background corrections and various instrument factors if these factors are included in the integrated intensities, and $P_{hkl}(\alpha, \beta)$ is the pole-density distribution function. Background correction can be done during the 2θ integration and will be discussed in Section 2.5.4.2.4. The pole figure is obtained by plotting the pole-density function based on the stereographic projection.

The pole-density function can be normalized such that it represents a fraction of the total diffracted intensity integrated over the pole sphere. The normalized pole-density distribution function is given by

$$g_{hkl}(\alpha, \beta) = \frac{2\pi P_{hkl}(\alpha, \beta)}{\int_0^{2\pi}\int_0^{\pi/2} P_{hkl}(\alpha, \beta)\cos\alpha \, \mathrm{d}\alpha \, \mathrm{d}\beta}. \tag{2.5.57}$$

The pole-density distribution function is a constant for a sample with a random orientation distribution. Assuming that the sample and instrument conditions are the same except for the pole-density distribution, we can obtain the normalized pole-density function by

$$g_{hkl}(\alpha, \beta) = \frac{I_{hkl}(\alpha, \beta)}{I_{hkl}^{\text{random}}(\alpha, \beta)}. \tag{2.5.58}$$

The integrated intensity from the textured sample without any correction can be plotted according to the stereographic projection as an 'uncorrected' pole figure. The same can be done for the sample with a random orientation distribution to form a 'correction' pole figure that contains only the factors to be corrected. The normalized pole figure is then obtained by dividing the 'uncorrected' pole figure by the 'correction' pole figure. This experimental approach is feasible only if a similar sample with a random orientation distribution is available.

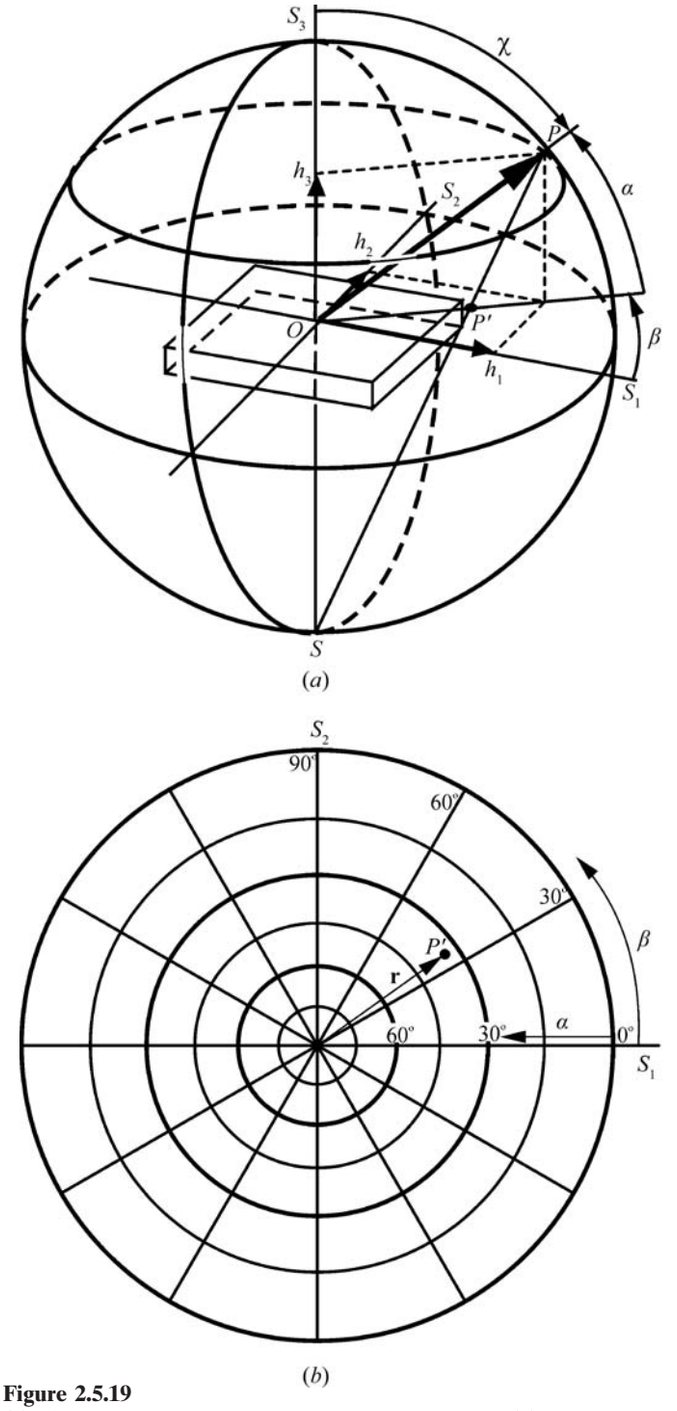

Figure 2.5.19
(*a*) Definition of pole direction angles α and β; (*b*) stereographic projection in a pole figure.

If the texture has a rotational symmetry with respect to an axis of the sample, the texture is referred to as a fibre texture and the axis is referred to as the fibre axis. The sample orientation containing the symmetry axis is referred to as the fibre axis. The fibre texture is mostly observed in two types of materials: metal wires or rods formed by drawing or extrusion, and thin films formed by physical or chemical deposition. The fibre axis is the wire axis for a wire and normal to the sample surface for thin films. Fibre texture can also be artificially formed by rotating a sample about its normal. If the fibre axis is aligned to the S_3 direction, the pole-density distribution function becomes independent of the azimuthal angle β. For samples with fibre texture, or artificially formed fibre texture by rotating, the pole-density function is conveniently expressed as a function of a single variable, $g_{hkl}(\chi)$. Here, χ is the angle between the sample normal and pole direction.

$$\chi = 90^\circ - \alpha \text{ or } \chi = \cos^{-1}|h_3|. \qquad (2.5.59)$$

The pole-density function for fibre texture can be expressed as a fibre plot. The fibre plot $g_{hkl}(\chi)$ can be calculated from the relative intensity of several peaks (He, 1992; He *et al.*, 1994) and artificial fibre texture can be achieved by sample spinning during data collection.

2.5.4.2.3. *Data-collection strategy*

Since a one-dimensional pole-density mapping is created from each 2D frame, it is important to lay out a data-collection strategy so as to have the optimum pole-figure coverage and minimum redundancy in data collection. The pole-figure coverage can be simulated from the diffraction 2θ angle, detector swing angle, detector distance, goniometer angles and scanning steps. When a large 2D detector is placed close to the sample, it is possible to collect a pole figure with a single φ scan. Fig. 2.5.20(a) shows an example of a scheme generated by a single φ scan of 5° steps with a detector 10.5 cm in diameter and D = 7 cm. The data collected with a single exposure at $\varphi = 0^\circ$ would generate a one-dimensional pole figure as shown in the curve marked by A and B. The pole figure can be generated by a full-circle rotation of 360°. The pole density at the centre represents the diffraction vector perpendicular to the sample surface. It is important to have the pole-density information in the centre region of the pole figure, especially for fibre texture. The pole-figure angle at the centre is $\alpha = 90^\circ$, and the best strategy is to put point A at the centre of pole figure. That is

$$h_3^A = \sin\theta\cos\psi\sin\omega - \cos\theta\sin\gamma_A\cos\psi\cos\omega - \cos\theta\cos\gamma_A\sin\psi = 1. \qquad (2.5.60)$$

In some cases, a single φ scan is not enough to cover sufficient pole-figure angles because of a large detector distance or limited detector area, so it is necessary to collect a set of data with φ scans at several different sample tilt angles. Fig. 2.5.20(b) illustrates the data-collection scheme with a detector that is 10.5 cm in diameter and D = 10 cm for the (111) plane of a Cu thin film. In this case, each pole figure requires two φ scans at different sample orientations. The data-collection strategy should also be optimized for several crystallographic planes if all can be covered in a frame. The step size of the data-collection scan depends highly on the strength of the texture and the purpose of the texture measurements. For a weak texture, or quality control for metal parts, φ (or ω, or ψ) scan steps of 5° may be sufficient. For strong textures, such as thin films with epitaxial structure, scan steps of 1° or smaller may be necessary.

The effectiveness of two-dimensional data collection for a texture can be compared with that using a point detector with the data-collection strategy of the Cu thin film as an example. Fig. 2.5.20(c) shows the pole-figure data-collection strategy with a point detector. For the same pole-figure resolution, significantly more exposures are required with a point detector. Considering that several diffraction rings are measured simultaneously with a 2D detector, the pole-figure measurement is typically 10 to 100 times faster than with a point detector. Therefore, quantitative high-resolution pole-figure measurements are only practical with a 2D-XRD system (Bunge & Klein, 1996).

2.5.4.2.4. *Texture-data processing*

For a specific diffraction ring, 2θ is a constant or at least assumed to be constant for texture analysis, and the sample-orientation angles (ω, ψ, φ) for a frame are also constants. Therefore, the pole-density information is given by the diffraction-intensity distribution as a function of γ only, or $I = I(\gamma)$. Integration of the diffraction intensities in the 2θ direction converts 2D information into the function $I(\gamma)$.

Fig. 2.5.21(a) shows a 2D diffraction ring for texture analysis. The low and high background and diffraction-ring 2θ–γ range are defined by three boxes, noted as B_L, B_H and $I(\gamma)$, respectively. All three boxes have the same γ range from γ_1 to γ_2. The 2θ ranges for the diffraction ring, low background and high background should be determined based on the width of the 2θ peak and available background between adjacent peaks. Assuming a normal distribution, a 2θ range of 2 times the FWHM covers 98% of the intensity peak, and 3 times the FWHM covers more than 99.9%. The 2θ range should also be broad enough to cover the possible 2θ shifts caused by residual stresses in the sample. Fig. 2.5.21(b) is the 2θ profile integrated over the section $\Delta\gamma$ in Fig. 2.5.21(a). The background ranges on the low and high 2θ sides are given by $2\theta_{L1}$–$2\theta_{L2}$ and $2\theta_{H1}$–$2\theta_{H2}$, respectively. The 2θ-integrated diffraction intensities as a function of γ are plotted in Fig. 2.5.21(c). The background can be calculated and removed from the intensity values of the low and high backgrounds or ignored if the contribution of the background is very small.

2θ integration without a background correction can be

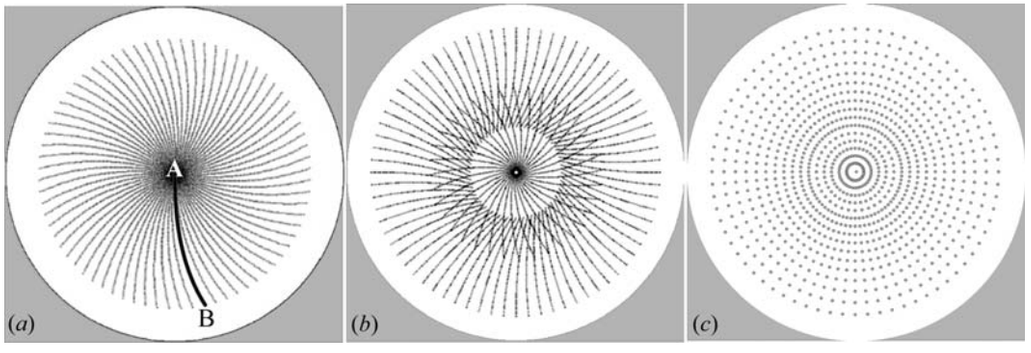

Figure 2.5.20
Data-collection strategy: (a) 2D detector with D = 7 cm; (b) 2D detector with D = 10 cm; (c) point detector.

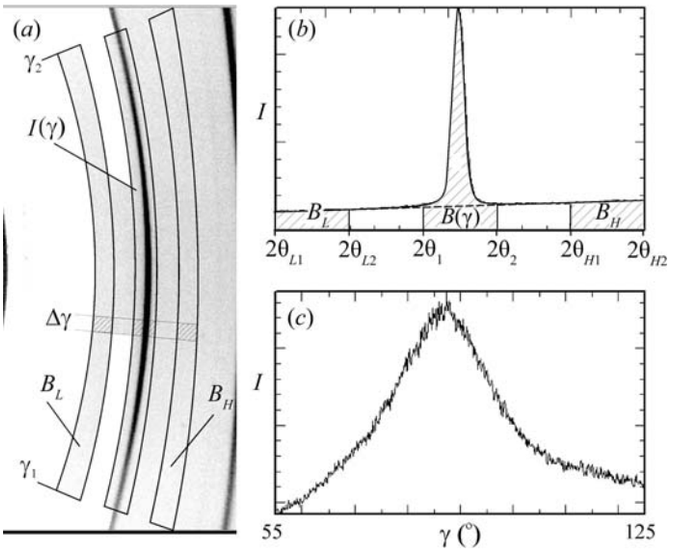

Figure 2.5.21
Pole-figure data processing: (*a*) a frame with the 2θ integration ranges for the (220) ring; (*b*) 2θ profile showing the background and peak; (*c*) integrated intensity distribution as a function of γ.

expressed as

$$I(\gamma) = \int_{2\theta_1}^{2\theta_2} J(2\theta, \gamma)\, \mathrm{d}(2\theta), \quad \gamma_1 \le \gamma \le \gamma_2. \tag{2.5.61}$$

A similar equation can be used for 2θ integration of the low and high backgrounds $B_L(\gamma)$ and $B_H(\gamma)$. Assuming a linear background change in the vicinity of the 2θ peak, the background under the peak, $B(\gamma)$, is then given by

$$B(\gamma) = B_L(\gamma)\frac{(2\theta_2 - 2\theta_1)(2\theta_{H2} + 2\theta_{H1} - 2\theta_2 - 2\theta_1)}{(2\theta_{L2} - 2\theta_{L1})(2\theta_{H2} + 2\theta_{H1} - 2\theta_{L2} - 2\theta_{L1})} + B_H(\gamma)\frac{(2\theta_2 - 2\theta_1)(2\theta_2 + 2\theta_1 - 2\theta_{L2} - 2\theta_{L1})}{(2\theta_{H2} - 2\theta_{H1})(2\theta_{H2} + 2\theta_{H1} - 2\theta_{L2} - 2\theta_{L1})}. \tag{2.5.62}$$

Then the background $B(\gamma)$ can be subtracted from the integrated intensity distribution $I(\gamma)$.

The algorithms of γ integration given in Section 2.5.4.2.3 can be easily modified for 2θ integration by exchanging γ and 2θ in the equations. Algorithms with solid-angle normalization should be used to get consistent integrated intensity over all areas of the detector. The 2θ-integrated intensity distribution can then be mapped onto a pole figure based on the fundamental equations (2.5.53) and (2.5.54). When a pole-figure pixel is overlapped by more than one data point from different scans, as shown in the region covered by two scans in Fig. 2.5.20(*b*), the average value should be mapped to that pole-figure pixel. Fig. 2.5.22(*a*) shows pole-density mappings on the pole figure. There are big gaps between the measured pole-density data points due to the large φ-scan steps of 5°.

All factors affecting relative intensities, such as Lorentz, polarization, air scattering, and Be-window and sample absorption, will have an effect on the measured pole densities for the pole figures. Some or all these corrections may be applied to the diffraction frames before 2θ integration if the texture study demands high accuracy in the relative pole densities. Among these factors, the most important factor is sample absorption, since data sets for pole figures are typically collected at several different incident angles. A ridge between the pole-density regions covered by two different incident angles may be observed if sample absorption is not properly corrected.

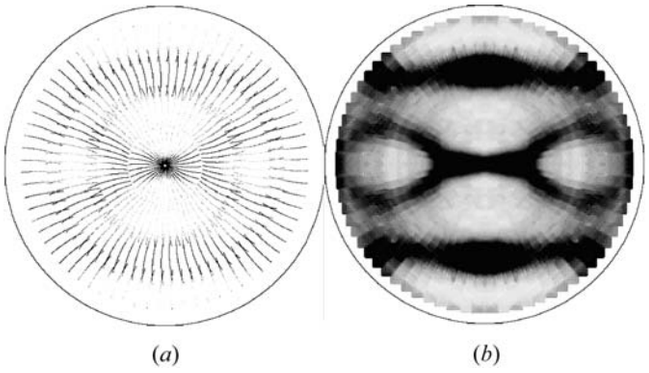

Figure 2.5.22
Pole-figure processing: (*a*) $I(\gamma)$ mapped to the pole figure; (*b*) Pole figure after interpolation and symmetry processing.

2.5.4.2.5. *Pole-figure interpolation and use of symmetry*

The pole figure is stored and displayed as a bitmap image. The pole-density data from the data set may not fill up all the pixels of the pole-figure image. In order to generate a smooth pole figure, the unmapped pixels are filled with values generated from the interpolation of the surrounding pixels. A linear interpolation within a defined box is sufficient to fill the unmapped pixels. The size of the box should be properly chosen. A box that is too small may not be able to fill all unmapped pixels and a box that is too big may have a smearing effect on the pole figure, especially if a sharp pole figure is processed. All the gaps between the measured pole-density points are filled after this interpolation. For a sample with sharp texture, smaller φ-scan steps should be used.

All pole figures possess symmetry as a consequence of the Laue symmetry of the crystallites in the sample. This symmetry can be used to fill in values for pixels in the pole figure for which data were not measured, or to smooth the pole figure. For example, orthorhombic materials exhibit *mmm* symmetry, thus one needs to collect only an octant or quadrant of the pole sphere to generate the entire pole figure. The pole figures of materials with higher symmetry may be treated by using lower symmetry in the processing. For instance, one can use 2/*m* or *mmm* symmetry for hexagonal materials and *mmm* for cubic materials. In symmetry processing, all the symmetry-equivalent pole-figure pixels are filled by the average value of the measured pixels. For the unmeasured pole-figure pixels, this symmetry processing fills in a value from the average of all the equivalent pixels. For the measured pixels, this average processing serves as a smoothing function. Fig. 2.5.22(*b*) shows the results after both interpolation and use of symmetry.

2.5.4.2.6. *Orientation relationship*

A 2D-XRD system can measure texture from a sample containing a single phase, multiple phases or single crystals. The orientation relationship between different phases, or thin films and substrates, can be revealed because data are collected from all phases of the sample simultaneously. One example is the measurement of pole figures for a magnetron sputter-deposited Cu film on an Si wafer (He *et al.*, 2005). Fig. 2.5.23 shows the overlapped pole figures of the Cu (111) film and Si (400) substrate in a 2D pole figure (*a*) and 3D surface plot (*b*). The three sharp spots from the (400) spots of the Si wafer show the wafer cut orientation of (111). The Cu (111) pole density maxi-

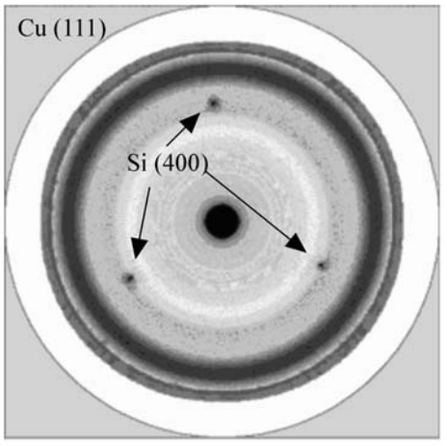

(*a*)

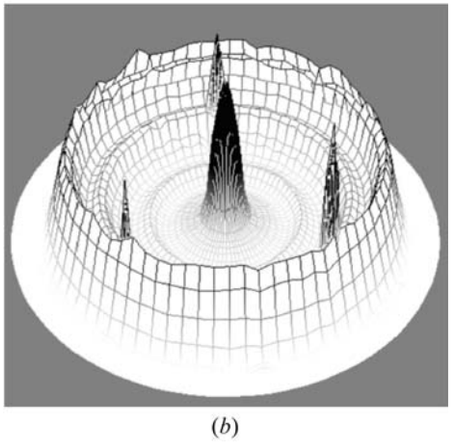

(*b*)

Figure 2.5.23
Combined pole figure of a Cu (111) film on an Si (400) substrate: (*a*) regular 2D projection; (*b*) 3D surface plot.

mized in the centre of the pole figure shows a strong (111) fibre texture. The orientation relationship between the film fibre axis and the substrate is clearly described by the combined pole figures. For samples containing multiple thin-film layers, the orientation relationships between the different layers of the films and substrate can be revealed by superimposing their pole figures.

2.5.4.3. *Stress measurement*

When a solid material is elastically deformed by a force, each crystallite in it changes shape or size. Assuming that the stresses in each crystallite represent the stresses in the solid, the stresses can be measured by measuring the lattice d-spacing changes in the crystallites. These d-spacing changes can be measured by the changes in diffraction-peak positions based on Bragg's law. In this case, the d-spacing serves as a gauge of the deformation. Stress measurement by X-ray diffraction is typically done using a point detector or line detector (Walter, 1971; James & Cohen, 1980; Noyan & Cohen, 1987; Lu, 1996); this will be referred to as the conventional method. The stress or stress tensor is calculated from many strain measurements from diffraction-peak 2θ shifts of a specific lattice-plane family. With a point or line detector, only a small cross section of the diffraction cone is measured at one sample orientation (ψ, φ). Compared to using a conventional detector, 2D detectors have many advantages in stress measurement (Borgonovi, 1984; Korhonen *et al.*, 1989; Yoshioka & Ohya, 1992; Fujii & Kozaki, 1993; He & Smith, 1997; Kämpfe *et al.*, 1999; Hanan *et al.*, 2004). Since a 2D diffraction pattern covers the whole or a large portion of the diffraction rings, it can be used to measure stress with higher accuracy and can be collected in a shorter time than a conventional diffraction pattern, especially when dealing with highly textured materials, large grain sizes, small sample areas, weak diffraction, stress mapping and stress-tensor measurement. The 2D method for stress measurement is based on the fundamental relationship between the stress tensor and the diffraction-cone distortion (He & Smith, 1997; He, 2000; European Standard, 2008).

There are two kinds of stresses, which depend on the source of the loading forces that produce them. One kind is applied stress, caused by external forces acting on the solid object. Applied stress changes when the loading forces change and it disappears once the forces are removed. The stresses measured by X-ray diffraction method are mostly residual stresses. Residual stress is caused by internal forces between different parts of a solid body. Residual stress exists without external forces or remains after the external forces have been removed. The net force and moment on a solid body in equilibrium must be zero, so the residual stresses in the body must be balanced within the body. This means that a compressive stress in one part of the body must come with a tensile stress in another part of the body. For example, the residual stress in a thin film is balanced by the stresses in the substrate. When residual stress in a solid body is mentioned it typically refers to a specific location.

Residual stresses are generally categorized as macroscopic or microscopic depending on the range over which the stresses are balanced. The macroscopic residual stress is the stress measured over a large number of grains. This kind of stress can be measured by X-ray diffraction through the shift of the Bragg peaks. The microscopic stress is the stress measured over one or a few grains, or as small a range as micro- or nanometres. This kind of stress alone will not cause a detectable shift of diffraction peaks, but is reflected in the peak profiles. In this chapter, we will focus on the X-ray diffraction method for stress measurement at the macroscopic level.

2.5.4.3.1. *Stress and strain relation*

Stress is a measure of the deforming force applied to a solid per unit area. The stress on an elemental volume in the sample coordinates S_1, S_2, S_3 contains nine components, given by

$$\sigma_{ij} = \begin{bmatrix} \sigma_{11} & \sigma_{12} & \sigma_{13} \\ \sigma_{21} & \sigma_{22} & \sigma_{23} \\ \sigma_{31} & \sigma_{32} & \sigma_{33} \end{bmatrix}. \tag{2.5.63}$$

A component is normal stress when the two indices are identical, or shear stress when the two indices differ. The group of the nine stress components is called the stress tensor. The stress tensor is a tensor of the second order. Under equilibrium conditions, the shear components must maintain the following relations:

$$\sigma_{12} = \sigma_{21},\ \ \sigma_{23} = \sigma_{32} \text{ and } \sigma_{31} = \sigma_{13}. \tag{2.5.64}$$

Therefore, only six independent components define the stress state in a solid. The following stress states are typically measured:

Uniaxial: all stress components are zero except one normal stress component.

Biaxial: all nonzero components are within the S_1S_2 plane.

Biaxial with shear: $\sigma_{33} = 0$, all other components are not necessarily zero.

Equibiaxial: a special case of biaxial stress where $\sigma_{11} = \sigma_{22} = \sigma$.

Triaxial: all components are not necessarily zero.

Equitriaxial: a special case of triaxial stress where $\sigma_{11} = \sigma_{22} = \sigma_{33} = \sigma$.

Strain is a measure of the resulting deformation of a solid body caused by stress. Strain is calculated from the change in the size and shape of the deformed solid due to stress. Analogous to normal stresses and shear stresses are normal strains and shear strains. The normal strain is calculated from the change in length of the solid body along the corresponding normal stress direction. Like the stress tensor, the strain tensor contains nine components:

$$\varepsilon_{ij} = \begin{bmatrix} \varepsilon_{11} & \varepsilon_{12} & \varepsilon_{13} \\ \varepsilon_{21} & \varepsilon_{22} & \varepsilon_{23} \\ \varepsilon_{31} & \varepsilon_{32} & \varepsilon_{33} \end{bmatrix}. \tag{2.5.65}$$

The directions of all strain components are defined in the same way as for the stress tensor. Similarly, there are six independent components in the strain tensor. Strictly speaking, X-ray diffraction does not measure stresses directly, but strains. The stresses are calculated from the measured strains based on the elasticity of the materials. The stress–strain relations are given by the generalized form of Hooke's law:

$$\sigma_{ij} = C_{ijkl}\varepsilon_{kl}, \tag{2.5.66}$$

where C_{ijkl} are elastic stiffness coefficients. The stress–strain relations can also be expressed as

$$\varepsilon_{ij} = S_{ijkl}\sigma_{kl}, \tag{2.5.67}$$

where S_{ijkl} are the elastic compliances. For most polycrystalline materials without texture or with weak texture, it is practical and reasonable to consider the elastic behaviour to be isotropic and the structure to be homogeneous on a macroscopic scale. In these cases, the stress–strain relationship takes a much simpler form. Therefore, the Young's modulus E and Poisson's ratio ν are sufficient to describe the stress and strain relations for homogeneous isotropic materials:

$$\begin{aligned} \varepsilon_{11} &= \frac{1}{E}[\sigma_{11} - \nu(\sigma_{22} + \sigma_{33})], \\ \varepsilon_{22} &= \frac{1}{E}[\sigma_{22} - \nu(\sigma_{33} + \sigma_{11})], \\ \varepsilon_{33} &= \frac{1}{E}[\sigma_{33} - \nu(\sigma_{11} + \sigma_{22})], \\ \varepsilon_{12} &= \frac{1+\nu}{E}\sigma_{12}, \quad \varepsilon_{23} = \frac{1+\nu}{E}\sigma_{23}, \quad \varepsilon_{31} = \frac{1+\nu}{E}\sigma_{31}. \end{aligned} \tag{2.5.68}$$

It is customary in the field of stress measurement by X-ray diffraction to use another set of macroscopic elastic constants, S_1 and $\frac{1}{2}S_2$, which are given by

$$\tfrac{1}{2}S_2 = (1+\nu)/E \ \text{ and } \ S_1 = -\nu/E. \tag{2.5.69}$$

Although polycrystalline materials on a macroscopic level can be considered isotropic, residual stress measurement by X-ray diffraction is done by measuring the strain in a specific crystal orientation of the crystallites that satisfies the Bragg condition. The stresses measured from diffracting crystallographic planes may have different values because of their elastic anisotropy. In such cases, the macroscopic elasticity constants should be replaced by a set of crystallographic plane-specific elasticity constants, $S_1^{\{hkl\}}$ and $\frac{1}{2}S_2^{\{hkl\}}$, called X-ray elastic constants (XECs). XECs for many materials can be found in the literature, measured or calculated from microscopic elasticity constants (Lu, 1996). In the case of materials with cubic crystal symmetry, the equations for calculating the XECs from the macroscopic elasticity constants $\frac{1}{2}S_2$ and S_1 are

$$\begin{aligned} \tfrac{1}{2}S_2^{\{hkl\}} &= \tfrac{1}{2}S_2[1 + 3(0.2 - \Gamma(hkl))\Delta] \\ S_1^{\{hkl\}} &= S_1 - \tfrac{1}{2}S_2[0.2 - \Gamma(hkl)]\Delta, \end{aligned} \tag{2.5.70}$$

where

$$\Gamma(hkl) = \frac{h^2k^2 + k^2l^2 + l^2h^2}{(h^2 + k^2 + l^2)^2} \ \text{ and } \ \Delta = \frac{5(A_{\rm RX} - 1)}{3 + 2A_{\rm RX}}.$$

In the equations for stress measurement hereafter, either the macroscopic elasticity constants $\frac{1}{2}S_2$ and S_1 or the XECs $S_1^{\{hkl\}}$ and $\frac{1}{2}S_2^{\{hkl\}}$ are used in the expression, but either set of elastic constants can be used depending on the requirements of the application. The factor of anisotropy ($A_{\rm RX}$) is a measure of the elastic anisotropy of a material (He, 2009).

2.5.4.3.2. *Fundamental equations*

Fig. 2.5.24 illustrates two diffraction cones for backward diffraction. The regular diffraction cone (dashed lines) is from the powder sample with no stress, so the 2θ angles are constant at all γ angles. The diffraction ring shown as a solid line is the cross section of a diffraction cone that is distorted as a result of stresses. For a stressed sample, 2θ becomes a function of γ and the sample orientation (ω, ψ, φ), *i.e.* $2\theta = 2\theta(\gamma, \omega, \psi, \varphi)$. This function is uniquely determined by the stress tensor. The strain measured by the 2θ shift at a point on the diffraction ring is $\varepsilon_{(\gamma,\omega,\psi,\varphi)}^{\{hkl\}}$, based on the true strain definition

$$\varepsilon_{(\gamma,\omega,\psi,\varphi)}^{\{hkl\}} = \ln\frac{d}{d_o} = \ln\frac{\sin\theta_o}{\sin\theta} = \ln\frac{\lambda}{2d_o\sin\theta}, \tag{2.5.71}$$

where d_o and θ_o are the stress-free values and d and θ are measured values from a point on the diffraction ring corresponding to (γ, ω, ψ, φ). The direction of $\varepsilon_{(\gamma,\omega,\psi,\varphi)}^{\{hkl\}}$ in the sample coordinates S_1, S_2, S_3 can be given by the unit-vector components h_1, h_2 and h_3. As a second-order tensor, the relationship between the measured strain and the strain-tensor components is then given by

$$\varepsilon_{(\gamma,\omega,\psi,\varphi)}^{\{hkl\}} = \varepsilon_{ij} \cdot h_i \cdot h_j. \tag{2.5.72}$$

The scalar product of the strain tensor with the unit vector in the above equation is the sum of all components in the tensor multiplied by the components in the unit vector corresponding to the first and the second indices. The expansion of this equation for i and j values of 1, 2 and 3 results in

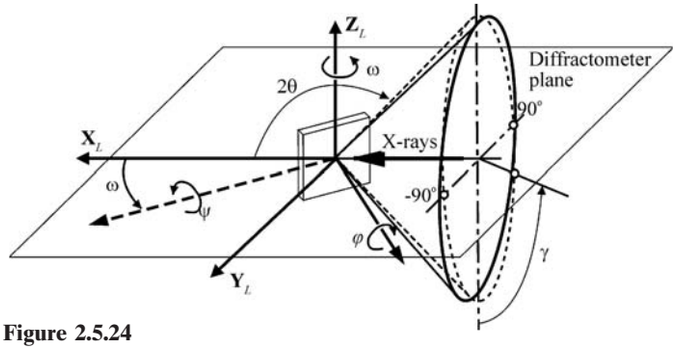

Figure 2.5.24
Diffraction-cone distortion due to stresses.

$$\varepsilon^{\{hkl\}}_{(\gamma,\omega,\psi,\varphi)} = h_1^2\varepsilon_{11} + 2h_1h_2\varepsilon_{12} + h_2^2\varepsilon_{22} + 2h_1h_3\varepsilon_{13} + 2h_2h_3\varepsilon_{23} + h_3^2\varepsilon_{33}. \tag{2.5.73}$$

Or, taking the true strain definition,

$$h_1^2\varepsilon_{11} + 2h_1h_2\varepsilon_{12} + h_2^2\varepsilon_{22} + 2h_1h_3\varepsilon_{13} + 2h_2h_3\varepsilon_{23} + h_3^2\varepsilon_{33} = \ln\left(\frac{\sin\theta_0}{\sin\theta}\right), \tag{2.5.74}$$

where θ_o corresponds to the stress-free d-spacing and θ are measured values from a point on the diffraction ring. Both θ and $\{h_1, h_2, h_3\}$ are functions of $(\gamma, \omega, \psi, \varphi)$. By taking γ values from 0 to 360°, equation (2.5.74) establishes the relationship between the diffraction-cone distortion and the strain tensor. Therefore, equation (2.5.74) is the fundamental equation for strain measurement with two-dimensional X-ray diffraction.

Introducing the elasticity of materials, one obtains

$$-\frac{\nu}{E}(\sigma_{11}+\sigma_{22}+\sigma_{33}) + \frac{1+\nu}{E}(\sigma_{11}h_1^2 + \sigma_{22}h_2^2 + \sigma_{33}h_3^2 + 2\sigma_{12}h_1h_2 + 2\sigma_{13}h_1h_3 + 2\sigma_{23}h_2h_3) = \ln\left(\frac{\sin\theta_0}{\sin\theta}\right) \tag{2.5.75}$$

or

$$S_1(\sigma_{11}+\sigma_{22}+\sigma_{33}) + \tfrac{1}{2}S_2(\sigma_{11}h_1^2 + \sigma_{22}h_2^2 + \sigma_{33}h_3^2 + 2\sigma_{12}h_1h_2 + 2\sigma_{13}h_1h_3 + 2\sigma_{23}h_2h_3) = \ln\left(\frac{\sin\theta_0}{\sin\theta}\right). \tag{2.5.76}$$

It is convenient to express the fundamental equation in a clear linear form:

$$p_{11}\sigma_{11} + p_{12}\sigma_{12} + p_{22}\sigma_{22} + p_{13}\sigma_{13} + p_{23}\sigma_{23} + p_{33}\sigma_{33} = \ln\left(\frac{\sin\theta_0}{\sin\theta}\right), \tag{2.5.77}$$

where p_{ij} are stress coefficients given by

$$p_{ij} = \begin{cases} (1/E)[(1+\nu)h_i^2 - \nu] = \tfrac{1}{2}S_2h_i^2 + S_1 & \text{if } i = j, \\ 2(1/E)(1+\nu)h_ih_j = 2\tfrac{1}{2}S_2h_ih_j & \text{if } i \neq j. \end{cases} \tag{2.5.78}$$

In the equations for the stress measurement above and hereafter, the macroscopic elastic constants $\frac{1}{2}S_2$ and S_1 are used for simplicity, but they can always be replaced by the XECs for the specific lattice plane $\{hkl\}$, $S_1^{\{hkl\}}$ and $\frac{1}{2}S_2^{\{hkl\}}$, if the anisotropic nature of the crystallites should be considered. For instance, equation (2.5.76) can be expressed with the XECs as

$$S_1^{\{hkl\}}(\sigma_{11}+\sigma_{22}+\sigma_{33}) + \tfrac{1}{2}S_2^{\{hkl\}}(\sigma_{11}h_1^2 + \sigma_{22}h_2^2 + \sigma_{33}h_3^2 + 2\sigma_{12}h_1h_2 + 2\sigma_{13}h_1h_3 + 2\sigma_{23}h_2h_3) = \ln\left(\frac{\sin\theta_0}{\sin\theta}\right). \tag{2.5.79}$$

The fundamental equation (2.5.74) may be used to derive many other equations based on the stress–strain relationship, stress state and special conditions. The fundamental equation and the derived equations are referred to as 2D equations hereafter to distinguish them from the conventional equations. These equations can be used in two ways. One is to calculate the stress or stress-tensor components from the measured strain (2θ-shift) values in various directions. The fundamental equation for stress measurement with 2D-XRD is a linear function of the stress-tensor components. The stress tensor can be obtained by solving the linear equations if six independent strains are measured or by linear least-squares regression if more than six independent measured strains are available. In order to get a reliable solution from the linear equations or least-squares analysis, the independent strain should be measured at significantly different orientations. Another function of the fundamental equation is to calculate the diffraction-ring distortion for a given stress tensor at a particular sample orientation (ω, ψ, φ) (He & Smith, 1998). The fundamental equation for stress measurement by the conventional X-ray diffraction method can also be derived from the 2D fundamental equation (He, 2009).

2.5.4.3.3. *Equations for various stress states*

The general triaxial stress state is not typically measured by X-ray diffraction because of low penetration. For most applications, the stresses in a very thin layer of material on the surface are measured by X-ray diffraction. It is reasonable to assume that the average normal stress in the surface-normal direction is zero within such a thin layer. Therefore, $\sigma_{33} = 0$, and the stress tensor has five nonzero components. In some of the literature this stress state is denoted as triaxial. In order to distinguish this from the general triaxial stress state, here we name this stress state as the 'biaxial stress state with shear'. In this case, we can obtain the linear equation for the biaxial stress state with shear:

$$p_{11}\sigma_{11} + p_{12}\sigma_{12} + p_{22}\sigma_{22} + p_{13}\sigma_{13} + p_{23}\sigma_{23} + p_{\rm ph}\sigma_{\rm ph} = \ln\left(\frac{\sin\theta_0}{\sin\theta}\right), \tag{2.5.80}$$

where the coefficient $p_{\rm ph} = \frac{1}{2}S_2 + 3S_1$ and $\sigma_{\rm ph}$ is the pseudo-hydrostatic stress component introduced by the error in the stress-free d-spacing. In this case, the stresses can be measured without the accurate stress-free d-spacing, since this error is included in $\sigma_{\rm ph}$. The value of $\sigma_{\rm ph}$ is considered as one of the unknowns to be determined by the linear system. With the measured stress-tensor components, the general normal stress (σ_φ) and shear stress (τ_φ) at any arbitrary angle φ can be given by

$$\sigma_\varphi = \sigma_{11}\cos^2\varphi + \sigma_{12}\sin 2\varphi + \sigma_{22}\sin^2\varphi, \tag{2.5.81}$$

$$\tau_\varphi = \sigma_{13}\cos\varphi + \sigma_{23}\sin\varphi. \tag{2.5.82}$$

Equation (2.5.81) can also be used for other stress states by removing the terms for stress components that are zero. For instance, in the biaxial stress state $\sigma_{33} = \sigma_{13} = \sigma_{23} = 0$, so we have

$$p_{11}\sigma_{11} + p_{12}\sigma_{12} + p_{22}\sigma_{22} + p_{\rm ph}\sigma_{\rm ph} = \ln\left(\frac{\sin\theta_0}{\sin\theta}\right). \tag{2.5.83}$$

In the 2D stress equations for any stress state with $\sigma_{33} = 0$, we can calculate stress with an approximation of d_o (or $2\theta_o$). Any error in d_o (or $2\theta_o$) will contribute only to a pseudo-hydrostatic term $\sigma_{\rm ph}$. The measured stresses are independent of the input d_o (or $2\theta_o$) values (He, 2003). If we use d_0' to represent the initial input, then the true d_o (or $2\theta_o$) can be calculated from $\sigma_{\rm ph}$ with

$$d_0 = d_0' \exp\left(\frac{1-2\nu}{E}\sigma_{\rm ph}\right), \tag{2.5.84}$$

$$\theta_0 = \arcsin\left[\sin\theta_0' \exp\left(\frac{1-2\nu}{E}\sigma_{\rm ph}\right)\right]. \tag{2.5.85}$$

Care must be taken that the $\sigma_{\rm ph}$ value also includes the measurement error. If the purpose of the experiment is to

determine the stress-free d-spacing d_o, the instrument should be first calibrated with a stress-free standard of a similar material.

2.5.4.3.4. *Data-collection strategy*

The practice of stress analysis with 2D-XRD involves the selection of the diffraction-system configuration and the data-collection strategy, frame correction and integration, and stress calculation from the processed data points. Most concepts and strategies developed for a conventional diffractometer are still valid for 2D-XRD. We will focus on the new concepts and practices due to the nature of the 2D detectors.

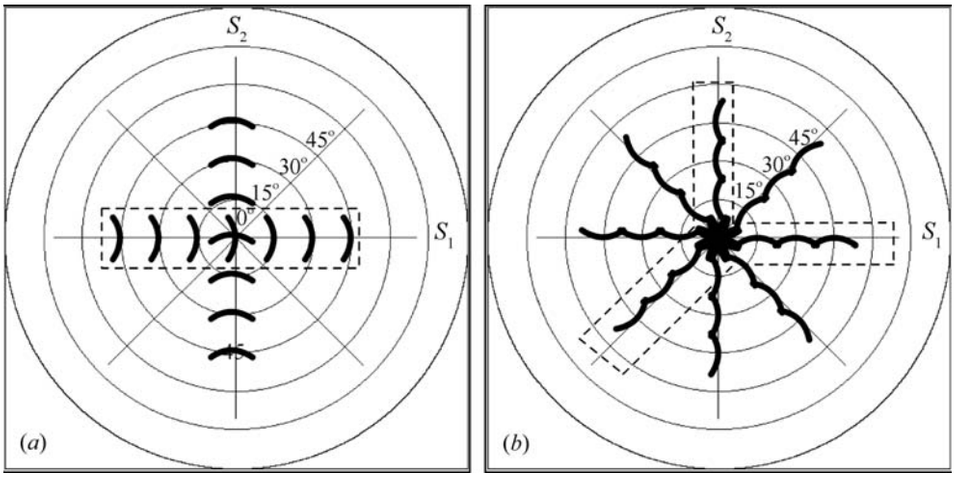

Figure 2.5.25
Data-collection strategy schemes: (*a*) $\omega + \varphi$ scan; (*b*) $\psi + \varphi$ scan.

The diffraction vector is in the normal direction to the measured crystalline planes. It is not always possible to have the diffraction vector in the desired measurement direction. In reflection mode, it is easy to have the diffraction vector normal to the sample surface, or tilted away from the normal, but impossible to have the vector on the surface plane. The stress on the surface plane, or biaxial stress, is calculated by elasticity theory from the measured strain in other directions. The final stress-measurement results can be considered as an extrapolation from the measured values. In the conventional $\sin^2\psi$ method, several ψ-tilt angles are required, typically at 15° steps from −45° to +45°. The same is true with a 2D-XRD system. The diffraction vectors corresponding to the data scan can be projected onto a 2D plot in the same way as the pole-density distribution in a pole figure. The 2D plot is called a data-collection strategy scheme.

By evaluating the scheme, one can generate a data-collection strategy suitable for the measurement of the intended stress components. Fig. 2.5.25 illustrates two schemes for data collection. In the bisecting condition ($\omega = \theta$ or $\theta_1 = \theta$ and $\psi = 0°$), the trace of the diffraction vector falls in the vicinity of the scheme centre. Either an ω tilt or a ψ tilt can move the vectors away from the centre. The circles on the scheme are labelled with the tilt angle of 15°, 30° and 45°. Scheme (*a*) is for an ω tilt of 0°, ±15°, ±30° and ±45° with the φ angle at 0° and 90°. It is obvious that this set of data would be suitable for calculating the biaxial-stress tensor. The data set with $\varphi = 0°$, as shown within the box enclosed by the dashed lines, would be sufficient on its own to calculate σ_{11}. Since the diffraction-ring distortion at $\varphi = 0°$ or $\varphi = 90°$ is not sensitive to the stress component σ_{12}, strategy (*a*) is suitable for the equibiaxial stress state, but is not able to determine σ_{12} accurately. In scheme (*b*), the ψ scan covers 0° to 45° with 15° steps at eight φ angles with 45° intervals. This scheme produces comprehensive coverage on the scheme chart in a symmetric distribution. The data set collected with this strategy can be used to calculate the complete biaxial-stress tensor components and shear stress (σ_{11}, σ_{12}, σ_{22}, σ_{13}, σ_{23}). The scheme indicated by the boxes enclosed by the dashed lines is a time-saving alternative to scheme (*b*). The rings on two φ angles are aligned to S_1 and S_2 and the rings on the third φ angle make 135° angles to the other two arrays of rings. This is analogous to the configuration of a stress-gauge rosette. The three φ angles can also be separated equally by 120° steps. Suitable schemes for a particular experiment should be determined by considering the stress components of interest, the goniometer, the sample size, the detector size and resolution, the desired measurement accuracy and the data-collection time.

2.5.4.3.5. *Data integration and peak evaluation*

The purpose of data integration and peak evaluation is to generate a set of data points along distorted diffraction rings. Data integration for stress analysis is γ integration over several defined segments so as to generate diffraction profiles representing the corresponding segments. The peak position can be determined by fitting the diffraction profile to a given analytic function. Fig. 2.5.26 illustrates data integration over a diffraction frame. The total integration region is defined by $2\theta_1$, $2\theta_2$, γ_1 and γ_2. The integration region is divided into segments given by $\Delta\gamma$. One data point on the distorted diffraction ring is generated from each segment. The γ value in the centre (denoted by the dot-dashed line) of each segment is taken as the γ value of the data point. γ integration of the segment produces a diffraction profile and the 2θ value is determined from the profile. The number of segments and the segment size ($\Delta\gamma$) are selected based on the quality of the data frame. The larger the segment size $\Delta\gamma$ is, the better the integrated diffraction profile as more counts are being integrated. γ integration also produces a smearing effect on the diffraction-ring distortion because the counts collected within the segment size $\Delta\gamma$ are considered as a single γ value at the segment

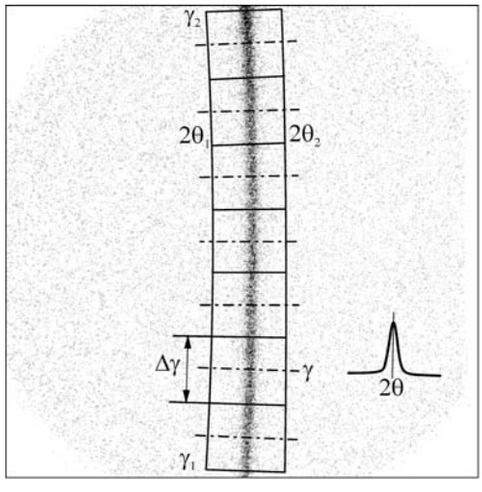

Figure 2.5.26
Data integration for stress measurement.

centre. The 2θ shift in the segment is averaged. The segment size $\Delta\gamma$ should be sufficient to produce a smooth diffraction profile, but not so large as to introduce too much smearing. For data frames containing high pixel counts, the integration segment can be small, *e.g.* $\Delta\gamma \leq 2^\circ$, and still have a smooth profile for each segment. For data frames having low pixel counts, for example the frames collected from a micron-sized area, from a sample with large grains or with a short data-collection time, it is critical to choose a sufficiently large segment size. The segment size can be determined by observing the smoothness of the integrated profile.

Peak evaluation in each segment can be done using the same algorithm used in the conventional method. The corrections to the integrated profiles are performed before or during the peak evaluation. Absorption correction eliminates the influence of the irradiated area and the diffraction geometry on the measured intensity distribution. The absorption for a given material and radiation level depends on the incident angle to the sample and the reflected angle from the sample. For 2D-XRD, the reflected angle is a function of γ for each frame. The polarization effect is also a function of γ. Therefore, the correction for polarization and absorption should be applied to the frame before integration. (Details of these corrections were discussed in Section 2.5.4.3.4.) The polarization and absorption correction is not always necessary if the error caused by absorption can be tolerated for the application, or if the data-collection strategy involves only ψ and φ scans.

In most cases, $K\alpha$ radiation is used for stress measurement, in which case the weighted average wavelength of $K\alpha_1$ and $K\alpha_2$ radiation is used in the calculations. For samples with a broad peak width, diffraction of $K\alpha_1$ and $K\alpha_2$ radiation is merged together as a single peak profile, and the profile can be evaluated as if there is a single $K\alpha$ line without introducing much error to the measured d-spacing. For samples with a relatively narrow peak width, the diffraction profile shows strong asymmetry or may even reveal two peaks corresponding to the $K\alpha_1$ and $K\alpha_2$ lines, especially at high 2θ angles. In this case the profile fitting should include contributions from both the $K\alpha_1$ and $K\alpha_2$ lines. It is common practice to use the peak position from the $K\alpha_1$ line and the $K\alpha_1$ wavelength to calculate the d-spacing after $K\alpha_2$ stripping.

Background correction is necessary if there is a strong background or the peak-evaluation algorithms are sensitive to the background, such as in $K\alpha_2$ stripping, peak fitting, and peak-intensity and integrated-intensity evaluations. Background correction is performed by subtracting a linear intensity distribution based on the background intensities at the lower 2θ side and the higher 2θ side of the diffraction peak. The background region should be sufficiently far from the 2θ peak so that the correction will not truncate the diffraction profile. The 2θ ranges of the low background and high background should be determined based on the width of the 2θ peak and available background in the profile. Based on a normal distribution, a 2θ range of 2 times the FWHM covers 98% of the peak intensity, and 3 times the FWHM covers more than 99.9%, so the background intensity should be determined at more than 1 to 1.5 times the FWHM away from the peak position. The background correction can be neglected for a profile with a low background or if the error caused by the background is tolerable for the application. The peak position can be evaluated by various methods, such as gravity, sliding gravity, and profile fitting by parabolic, pseudo-Voigt or Pearson-VII functions (Lu, 1996; Sprauel & Michaud, 2002).

2.5.4.3.6. *Stress calculation*

The final data set after integration and peak evaluation should contain many data points describing the diffraction-ring shape for all collected frames. Each measured data point contains three goniometer angles (ω, ψ, φ) and the diffraction-ring position (γ, 2θ). The peak intensity or integrated intensity of the diffraction profile is another value to be determined and may be used in the stress calculation. In most cases the number of data points is more than the number of unknown stress components, so a linear least-squares method can be used to calculate the stresses. In a general least-squares regression, the residual for the ith data point is defined as

$$r_i = y_i - \hat{y}_i, \tag{2.5.86}$$

where y_i is the observed response value, $\hat{y}_i$ is the fitted response value and r_i is the residual, which is defined as the difference between the observed value and the fitted value. The summed square of residuals is given by

$$S = \sum_{i=1}^{n} r_i^2 = \sum_{i=1}^{n} (y_i - \hat{y}_i)^2, \tag{2.5.87}$$

where n is the number of data points and S is the sum-of-squares error to be minimized in the least-squares regression. For stress calculation, the observed response value is the measured strain at each data point,

$$y_i = \ln\left(\frac{\sin\theta_0}{\sin\theta_i}\right), \tag{2.5.88}$$

and the fitted response value is given by the fundamental equation as

$$\hat{y}_i = p_{11}\sigma_{11} + p_{12}\sigma_{12} + p_{22}\sigma_{22} + p_{13}\sigma_{13} + p_{23}\sigma_{23} + p_{33}\sigma_{33} + p_{\rm ph}\sigma_{\rm ph}, \tag{2.5.89}$$

where all possible stress components and stress coefficients are listed as a generalized linear equation. Since the response-value function is a linear equation of unknown stress components, the least-squares problem can be solved by a linear least-squares regression. In order to reduce the impact of texture, large grains or weak diffraction on the results of the stress determination, the standard error of profile fitting and the integrated intensity of each profile may be introduced as a weight factor for the least-squares regression (He, 2009).

2.5.4.3.7. *Comparison between the 2D method and the conventional method*

Stress measurement on a polycrystalline material by X-ray diffraction is based on the strain measurements in a single or in several sample orientations. Each measured strain is calculated from the average d-spacing of specific lattice planes $\{hkl\}$ over many crystallites (grains). A larger number of contributing crystallites gives better accuracy and sampling statistics (also referred to as particle statistics). The sampling statistics are determined by both the crystal structure and the instrumentation. The instrument window is mainly determined by the divergence of the incident X-ray beam. Lattice-plane families with high multiplicity will also effectively improve the sampling statistics. The number of contributing crystallites measured by a conventional diffractometer is limited by the sizes and divergences of the incident and diffracted beams to the point detector. In a two-

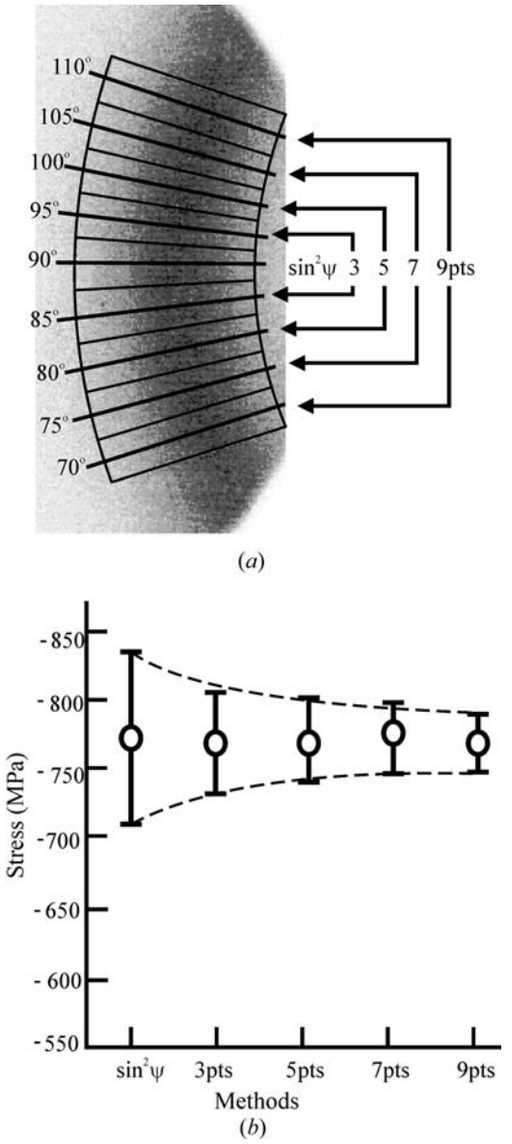

Figure 2.5.27
Stress calculation with the 2D method and the $\sin^2\psi$ method: (*a*) nine data points (abbreviated as pts) on the diffraction ring; (*b*) measured stress and standard deviation by different methods.

dimensional diffraction system, more crystallites can contribute to the diffraction because of the larger γ range.

An example of a stress calculation is provided by the measurement of the residual stress on the end surface of a carbon steel roller. One of the seven frames taken with an ω scan is shown in Fig. 2.5.27(*a*). The (211) ring covering the γ range 67.5 to 112.5° was used for stress analysis. First, the frame data were integrated along γ with an interval of $\Delta\gamma = 5°$. A total of nine diffraction profiles were obtained from γ integration. The peak position 2θ for each γ angle was then obtained by fitting the profile with a Pearson-VII function. A total of 63 data points can be obtained from the seven frames. The data points at $\gamma = 90°$ from seven frames, a typical data set for an ω diffractometer, were used to calculate the stress with the conventional $\sin^2\psi$ method. In order to compare the gain from having increased data points with the 2D method, the stress was calculated from 3, 5, 7 and 9 data points on each frame. The results from the conventional $\sin^2\psi$ method and the 2D method are compared in Fig. 2.5.27(*b*). The measured residual stress is compressive and the stress values from different methods agree very well. With the data taken from the same measurement (seven frames), the 2D method gives a lower standard error and the error decreases with increasing number of data points from the diffraction ring.

2.5.4.4. *Quantitative analysis*

2.5.4.4.1. *Crystallinity*

The crystallinity of a material influences many of its characteristics, including mechanical strength, opacity and thermal properties. Crystallinity measurement provides valuable information for both materials research and quality control in materials processing. The diffraction pattern from a material containing both amorphous and crystalline solids has a broad feature from the amorphous phase and sharp peaks from the crystalline phase. The weight percentage of the crystalline phases in a material containing both crystalline and amorphous phases can be determined by X-ray diffraction (Chung & Scott, 1973; Alexander, 1985; Murthy & Barton, 2000; Kasai & Kakudo, 2005). Assuming that the X-ray scattering intensity from each phase in such a material is proportional to its weight percentage, and that the scattering intensities from all phases can be measured within a given 2θ range, the per cent crystallinity is given by

$$x_{\rm pc} = 100\% \frac{I_{\rm crystal}}{I_{\rm crystal} + I_{\rm amorphous}}, \qquad (2.5.90)$$

where $x_{\rm pc}$ is the per cent crystallinity, $I_{\rm crystal}$ is the integrated intensity of all crystalline peaks and $I_{\rm amorphous}$ is the integrated intensity of the amorphous scattering. The accuracy of the measured per cent crystallinity depends on the integrated diffraction profile. Since most crystalline samples have a preferred orientation, it is very difficult to obtain a consistent measurement of crystallinity with a conventional diffractometer. Fig. 2.5.28 shows a 2D diffraction frame collected from an oriented polycrystalline sample. The diffraction is in transmission mode with the X-ray beam perpendicular to the plate sample surface. Fig. 2.5.28(*a*) shows a diffraction profile integrated from a horizontal region analogous to a profile collected with a conventional diffractometer. Only one peak from the crystalline phase can be observed in the profile. It is also possible that a different peak or no peak is measured if the sample is loaded in other orientations. Fig. 2.5.28(*b*) is the diffraction profile integrated from the region covering all peaks from the crystalline phase over almost all azimuthal angles. A total of four peaks from the crystalline phase are observed. This shows that a 2D-XRD system can measure per cent crystallinity more accurately and with more consistent results (Pople *et al.*, 1997; Bruker, 2000) than a conventional system.

2.5.4.4.2. *Crystallite size*

The size of the crystallites in a polycrystalline material has a significant effect on many of its properties, such as its thermal, mechanical, electrical, magnetic and chemical properties. X-ray diffraction has been used for crystallite-size measurement for many years. Most methods are based on diffraction-line broadening and line-profile analysis (Wilson, 1971; Klug & Alexander, 1974; Ungár, 2000). Another approach to crystallite-size measurement is based on the spotty diffraction rings collected with two-dimensional detectors when a small X-ray beam is used (Cullity, 1978; He, 2009). Line-profile analysis is based on the diffraction profile in the 2θ direction, while crystallite-size analysis with a spotty 2D diffraction pattern is based on the diffraction profile in the γ direction. The latter may be referred to as γ-profile analysis.

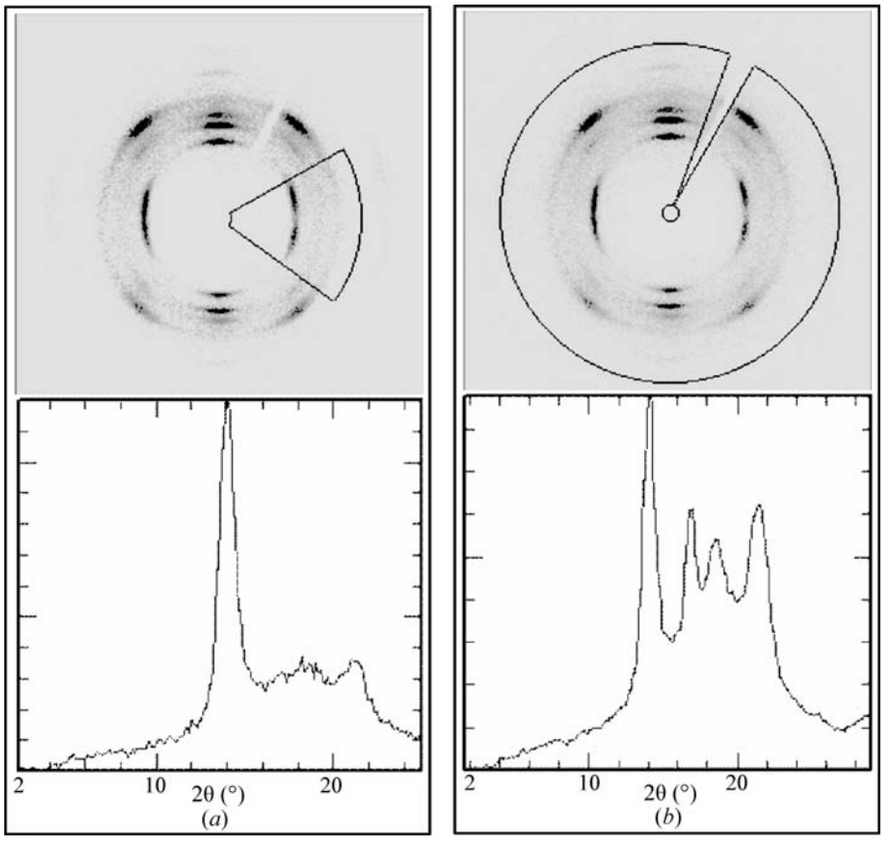

Figure 2.5.28
2D diffraction pattern from an oriented polycrystalline polymer sample. (*a*) Diffraction profile integrated from a horizontal region analogous to a profile collected with point detector. (*b*) Diffraction profile integrated from all parts of the 2D frame.

Fig. 2.5.29(*a*) shows a diffraction profile collected from gold nanoparticles and regular gold metal. The 2θ profile from the gold nanoparticles is significantly broader than the profile from regular gold metal. The crystallite size can be calculated by measuring the broadening and using the Scherrer equation:

$$B = \frac{C\lambda}{t\cos\theta}, \qquad (2.5.91)$$

where λ is the X-ray wavelength (in Å), B is the full width at half maximum (FWHM) of the peak (in radians) corrected for instrumental broadening and strain broadening, θ is the Bragg angle, C is a factor, typically from 0.9 to 1.0, depending on the crystallite shape (Klug & Alexander, 1974), and t is the crystallite size (also in Å). This equation shows an inverse relationship between crystallite size and peak-profile width. The wider the peak is, the smaller the crystallites. The 2θ diffraction profiles can be obtained either by using a conventional diffractometer with a point or line detector, or by γ integration from a diffraction pattern collected with 2D detector. When a 2D detector is used, a long sample-to-detector distance should be used to maximize the resolution. A small beam size and low convergence should also be used to reduce instrument broadening.

Fig. 2.5.29(*b*) shows a frame collected from an SRM660a (LaB_6) sample with a 2D-XRD system. The spotty diffraction rings are observed with average crystallite size of 3.5 μm. The number of spots in each diffraction ring is determined by the crystallite size and diffraction volume. Introducing a scaling factor covering all the numeric constants, the incident-beam divergence and the calibration factor for the instrument, we obtain an equation for the crystallite size as measured in reflection mode:

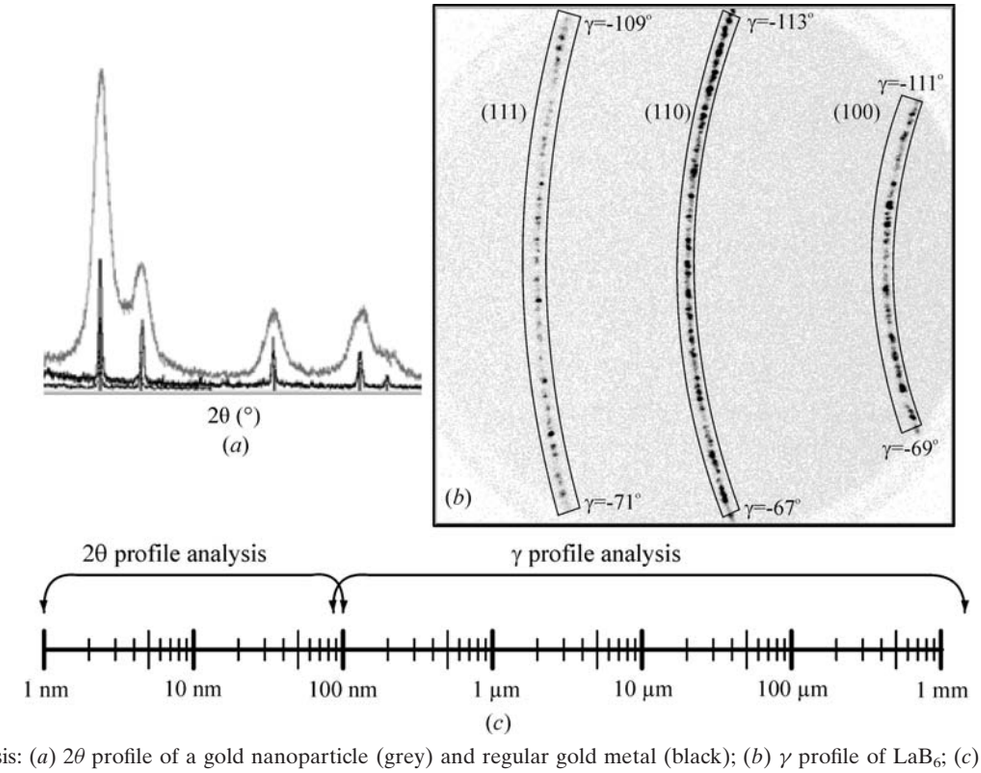

Figure 2.5.29
Crystallite-size analysis: (*a*) 2θ profile of a gold nanoparticle (grey) and regular gold metal (black); (*b*) γ profile of LaB_6; (*c*) measurement range.

$$d = k\left\{\frac{p_{hkl}b^2 \arcsin[\cos\theta \sin(\Delta\gamma/2)]}{\mu N_s}\right\}^{1/3}, \quad (2.5.92)$$

where d is the diameter of the crystallite particles, p_{hkl} is the multiplicity of the diffracting planes, b is the size of the incident beam (*i.e.* its diameter), $\Delta\gamma$ is the γ range of the diffraction ring, μ is the linear absorption coefficient and N_s is the number of spots within $\Delta\gamma$. For transmission mode, we have

$$d = k\left\{\frac{p_{hkl}b^2 t \arcsin[\cos\theta \sin(\Delta\gamma/2)]}{N_s}\right\}^{1/3}, \quad (2.5.93)$$

where t is the sample thickness. In transmission mode with the incident beam perpendicular to the sample surface, the linear absorption coefficient affects the relative scattering intensity, but not the actual sampling volume. In other words, all the sample volume irradiated by the incident beam contributes to the diffraction. Therefore, it is reasonable to ignore the absorption effect $\exp(\mu t)$ for crystallite-size analysis as long as the sample is thin enough for transmission-mode diffraction. The effective sampling volume reaches a maximum for transmission-mode diffraction when $t = 1/\mu$.

For both reflection and transmission,

$$k = \left(\frac{3\beta}{8\pi}\right)^{1/3}, \quad (2.5.94)$$

where β is the divergence of the incident beam. Without knowing the precise instrumental broadening, k can be treated as a calibration factor determined from the 2D diffraction pattern of a known standard. Since only a limited number of spots along the diffraction ring can be resolved, it can be seen from equation (2.5.94) that a smaller X-ray beam size and low-multiplicity peak should be used if a smaller crystallite size is to be determined.

Fig. 2.5.29(c) shows the measurement ranges of 2θ-profile and γ-profile analysis. The 2θ-profile analysis is suitable for crystallite sizes below 100 nm (1000 Å), while γ-profile analysis is suitable for crystallite sizes from as large as tens of μm down to 100 nm with a small X-ray beam size. By increasing the effective diffraction volume by translating the sample during data collection or multiple sample integration (or integrating data from multiple samples), the measurement range can be increased up to millimetres. Multiple sample integration can deal with large crystallite sizes without recalibration. The new calibration factor is given as

$$k_n = n^{1/3}k, \quad (2.5.95)$$

where n is the number of targets that are integrated. The number of crystallites can be counted by the number of intersections of the γ profile with a threshold line. Every two intersections of the γ profile with this horizontal line represents a crystallite. In order to cancel out the effects of preferred orientation and other material and instrumental factors on the overall intensity fluctuation along the γ profile, one can use a trend line fitted to the γ profile by a second-order polynomial. It is always necessary to calibrate the system with a known standard, preferably with a comparable sample geometry and crystallite size. For reflection mode, it is critical to have a standard with a comparable linear absorption coefficient so as to have similar penetration.

References

Alexander, L. E. (1985). *X-ray Diffraction Methods in Polymer Science*. Malabar: Krieger Publishing Company.

Allahkarami, M. & Hanan, J. C. (2011). *X-ray diffraction mapping on a curved surface*. *J. Appl. Cryst.* **44**, 1211–1216.

Arndt, U. W. (1986). *X-ray position-sensitive detectors*. *J. Appl. Cryst.* **19**, 145–163.

Arndt, U. W. (1990). *Focusing optics for laboratory sources in X-ray crystallography*. *J. Appl. Cryst.* **23**, 161–168.

Bergese, P., Bontempi, E., Colombo, I. & Depero, L. E. (2001). *Micro X-ray diffraction on capillary powder samples: a novel and effective technique for overcoming preferred orientation*. *J. Appl. Cryst.* **34**, 663–665.

Bhuvanesh, N. S. P. & Reibenspies, J. H. (2003). *A novel approach to micro-sample X-ray powder diffraction using nylon loops*. *J. Appl. Cryst.* **36**, 1480–1481.

Birkholz, M. (2006). *Thin Film Analysis by X-ray Scattering*, pp. 191–195. Weinheim: Wiley-VCH.

Blanton, T. N. (1994). *X-ray diffraction orientation studies using two-dimensional detectors*. *Adv. X-ray Anal.* **37**, 367–373.

Blanton, T. N. (2003). *X-ray film as a two-dimensional detector for X-ray diffraction analysis*. *Powder Diffr.* **18**, 91–98.

Bloomer, A. C. & Arndt, U. W. (1999). *Experiences and expectations of a novel X-ray microsource with focusing mirror. I*. *Acta Cryst.* D**55**, 1672–1680.

Boesecke, P. (2007). *Reduction of two-dimensional small- and wide-angle X-ray scattering data*. *J. Appl. Cryst.* **40**, s423–s427.

Bontempi, E., Benedetti, D., Massardi, A., Zacco, A., Borgese, L. & Depero, L. E. (2008). *Laboratory two-dimensional X-ray microdiffraction technique: a support for authentication of an unknown Ghirlandaio painting*. *Appl. Phys. A*, **92**, 155–159.

Borgonovi, G. M. (1984). *Determination of residual stress from two-dimensional diffraction pattern*. *Nondestructive Methods for Material Property Determination*, edited by C. O. Ruud & R. E. Green Jr, pp. 47–57. New York: Plenum Publishing Corporation.

Bourgeois, D., Moy, J. P., Svensson, S. O. & Kvick, Å. (1994). *The point-spread function of X-ray image-intensifiers/CCD-camera and imaging-plate systems in crystallography: assessment and consequences for the dynamic range*. *J. Appl. Cryst.* **27**, 868–877.

Bruker (2000). *Percent crystallinity in polymer*. Bruker AXS Lab Report No. L86-E00005.

Bunge, H. J. (1983). *Texture Analysis in Materials Science*. London: Butterworth.

Bunge, H. J. & Klein, H. (1996). *Determination of quantitative, high-resolution pole-figures with the area detector*. *Z. Metallkd.* **87**(6), 465–475.

Campbell, J. W., Harding, M. M. & Kariuki, B. (1995). *Spatial-distortion corrections, for Laue diffraction patterns recorded on image plates, modelled using polynomial functions*. *J. Appl. Cryst.* **28**, 43–48.

Cervellino, A., Giannini, C., Guagliardi, A. & Ladisa, M. (2006). *Folding a two-dimensional powder diffraction image into a one-dimensional scan: a new procedure*. *J. Appl. Cryst.* **39**, 745–748.

Chung, F. H. & Scott, R. W. (1973). *A new approach to the determination of crystallinity of polymers by X-ray diffraction*. *J. Appl. Cryst.* **6**, 225–230.

Cullity, B. D. (1978). *Elements of X-ray Diffraction*, 2nd ed. Reading, MA: Addison-Wesley.

Derewenda, Z. & Helliwell, J. R. (1989). *Calibration tests and use of a Nicolet/Xentronics imaging proportional chamber mounted on a conventional source for protein crystallography*. *J. Appl. Cryst.* **22**, 123–137.

Dickerson, M. B., Pathak, K., Sandhage, K. H., Snyder, R. L., Balachandran, U., Ma, B., Blaugher, R. D. & Bhattacharya, R. N. (2002). *Applications of 2D detectors in x-ray analysis*. *Adv. X-ray Anal.* **45**, 338–344.

Durst, R. D., Carney, S. N., Diawara, Y. & Shuvalov, R. (2002). *Readout structure and technique for electron cloud avalanche detectors*. US Patent No. 6, 340, 819.

Eatough, M. O., Rodriguez, M. A., Blanton, T. N. & Tissot, R. G. (1997). *A comparison of detectors used for microdiffraction applications*. *Adv. X-ray Anal.* **41**, 319–326.

Ercan, A., Tate, M. W. & Gruner, S. M. (2006). *Analog pixel array detectors*. *J. Synchrotron Rad.* **13**, 110–119.